High-performance unsymmetric 8-node hexahedral element in modeling nearly-incompressible soft tissues

Yu-Fei Wang [1], Song Cen[1, 2*], Chen-Feng Li [2, 3], Qun Zhang[4]

[1] *Department of Engineering Mechanics, School of Aerospace Engineering, Tsinghua University, Beijing 100084, China*

[2]*School of Mechanics & Engineering, Liaoning Technical University, Fuxin 123000, Liaoning, China*

[3] *Zienkiewicz Institute for Modelling, Data and AI, Swansea University, Swansea SA1 8EN, UK*

[4] *INTESIM (Dalian) CO., LTD., Dalian 116023, China*

Abstract

In biomechanics problems, the biological soft tissues are usually treated as anisotropic nearly-incompressible hyperelastic materials, but such complicated nonlinear material models often cause challenging problems of severe volumetric locking and instabilities in numerical simulations. In this paper, the recent unsymmetric 8-node, 24-DOF hexahedral solid element US-ATFH8 with different test and trial functions is modified for the analysis of anisotropic nearly-incompressible hyperelastic soft tissues. We use analytical trial functions (ATFs) to construct the incremental displacement fields which give the incremental deformation gradient. Specifically, the linear analytical general solutions for anisotropic elasticity and the consistent tangent

[*] Corresponding to: Song Cen, School of Mechanics & Engineering, Liaoning Technical University, Fuxin 123000, Liaoning, China.E-mail: censong@tsinghua.edu.cn

modulus are first introduced into the trial functions, which significantly improve the element performance. The total deformation gradient is obtained by multiplying the incremental deformation gradient by the deformation gradient, after which the Cauchy stresses can be directly calculated from a total-form constitutive equation relating to the deformation gradient. Numerical tests, including commonly used benchmarks and cardiac examples, demonstrate attractive properties of the proposed formulation in modeling anisotropic nearly-incompressible hyperelastic materials. It is robust and insensitive to mesh distortion, provides high accuracy with fast convergence rate, and overcomes locking problems in modelling nearly-incompressible materials.

Keywords: unsymmetric finite element, hyperelastic soft tissues, nearly-incompressible, finite deformation, analytical trial functions, hexahedral element

1. Introduction

In biomechanics and related applications, soft tissues are commonly treated as anisotropic hyperelastic materials [1-4]. For example, HGO [5-7] and Fung-type [8-12] models are commonly used to model arterial wall tissue and cardiac tissue, respectively. These two models have already been implemented in some commercial finite element software platforms [13]. The research of finite element simulation of biological soft tissues has been growing for the past decades, but the study on how to improve the performance of computational modeling is much limited. Land *et al*. [14] provided a series of benchmark problems for the verification of related solvers. Some stabilized methods were developed to deal with the nearly-incompressible condition and locking problems. Campos *et al*. [15] proposed a preconditioned augmented Lagrangian formulate to handle the nearly-incompressible condition. A locking-free finite element formulation in terms of Kirchhoff stress, displacement, and pressure was introduced by Chavan [16] and has been adopted in the study of cardiac electromechanics [17, 18]. More recently, Patrick [19] proposed a mixed formulation for incompressible hyperelasticity, in which an augmented Lagrangian preconditioner was added to the solutions of the benchmark problems of cardiac mechanics. A common drawback of these stabilized methods is that the stabilization constant must be chosen tentatively [20-22]. Furthermore, modelling biological soft tissues often leads to large scale numerical systems with high computational cost. The high-order element with pressure DOFs [23-27] can effectively deal with incompressible condition, but it also

significantly increases the amount of calculation and complexity. Smoothed finite element method [28] and immersed boundary-finite element method [29] are also applied to biomechanical problems , which show good accuracy and computational efficiency. Besides the above finite element formulations, the penalty methods [30-34] are also popular to enforce incompressibility in cardiac mechanics models. A pure displacement-based finite element formulation for nearly-incompressible cardiac mechanics was presented by Hadjicharalambous *et al* [35]. It shows that, without the additional variables, direct discretization of the penalized form can still produce similar convergence behavior to the mixed formulations.

Compared to high-order elements, the low-order pure displacement-based nonlinear finite elements often suffer from such numerical issues as locking and ill-conditioned stiffness matrix while the incompressible limit is approached. However, the low-order elements are attractive in large-scale problems due to simplicity and efficiency and as such a number of formulations have been proposed to enable the use of low-order elements near the incompressible limit. These include the B-bar methodology [36, 37], the F-bar technique [38-40], J-bar method [41], reduce integration scheme [42, 43], selective reduced integration scheme [44], the enhanced assumed strain elements [45, 46], the corotational incompatible modes approach [47], and multi-field formulations [48], among others. However, the presence of extremely large strains leads to distorted meshes, which typically requires adaptive mesh refinement to obtain acceptable solutions. As a result, using low-order finite elements

in large-strain analysis of quasi-incompressible materials remains an outstanding challenge.

Rajendran *et al*. [49, 50] first proposed the high-order unsymmetric finite element method to improve the performance of the pure displacement element for 2D and 3D problems with mesh distortion. He used two different sets of shape functions (conventional isoparametric shape functions and metric shape functions) to construct the test and trial functions, respectively. The higher-order monomial terms in the metric shape functions ensure good performance under mesh distortion. These elements were successfully extended to nonlinear analysis [51]. However, this method is not applicable to low-order elements, due to the inherent direction dependence and interpolation failure. In order to achieve high-performance in low-order elements, Cen *et al*. [52-56] incorporated the ATFs [57, 58] and the local natural coordinates [59, 60] into the unsymmetric finite element formulations. The test functions still come from the conventional isoparametric shape functions whilst the trial functions are constructed by the ATFs under local natural coordinates. The resulting plane 4-node, 8-DOF quadrilateral element US-ATFQ4 and 3D 8-node, 24-DOF hexahedral element US-ATFH8 exhibit high precision in both regular and distorted meshes, and they do not suffer locking problems. More recently, the unsymmetric finite elements based on ATFs method were extended to isotropic hyperelastic finite deformation analysis in both 2D [61] and 3D [62] problems. Besides, the incompatible modes were also extended into unsymmetric finite element analysis to construct low-order elements [63-66], which

also show good performance under mesh distortion.

The use of ATFs, namely the homogenous solutions for linear elasticity governing equations, is usually limited linear elastic situations [67], whilst through an incremental scheme they are greatly effective in elements US-ATFQ4 and US-ATFH8 for geometrical nonlinear analysis and isotropic hyperelastic problems. In elements US-ATFQ4 and US-ATFH8, the isotropic analytical homogeneous solutions were adopted to construct the ATFs. However, for hyperelastic soft tissues, anisotropic analytical homogeneous solutions are needed. It is worth investigating whether the unsymmetric element US-ATFH8 still possesses high distortion resistance and high precision for anisotropic nearly incompressible hyperelastic analysis.

In this paper, a new element strategy is proposed to model anisotropic nearly-incompressible hyperelastic soft tissues subjected to finite deformation. It is noted that viscoelastic effects [68-71] are not considered in the present formulation. The article is organized as follows. First, Section 2 recaps the deformation and the anisotropic hyperelastic material model, after which the unsymmetric finite formulation is illustrated in detail in Section 3. Then, in Section 4, various test examples are presented to evaluate the performance of the new formulation. Finally, concluding remarks and future extensions of are presented in Section 5.

2. Finite Deformation Hyperelasticity

This section first briefly reviews the mathematical foundation of deformation. As the topic of this paper is about anisotropic hyperelastic material, the typical Fung-type

strain-energy function in terms of the components of strain is explained, and the related stress response is also presented in preparation for the construction of finite element formulation.

2.1 Finite deformation

As shown in **Figure 1**, ${}^0B$ is the reference configuration of a continuous body which is assumed to be stress-free. The finite deformation of this body transforms a typical material point ${}^0\mathbf{x} \in {}^0B$ to the position ${}^t\mathbf{x} = {}^t\mathbf{x}\left({}^0\mathbf{x}\right) \in {}^tB$ in the deformed configuration ${}^tB$. The deformation process can be described by the deformation gradient ${}^t\mathbf{F} = \partial {}^t\mathbf{x} / \partial {}^0\mathbf{x}$, while the determinant ${}^tJ$ of ${}^t\mathbf{F}$, i.e., the local volume ratio, is given by ${}^tJ\left({}^t\mathbf{F}\right) = \det[{}^t\mathbf{F}]$.

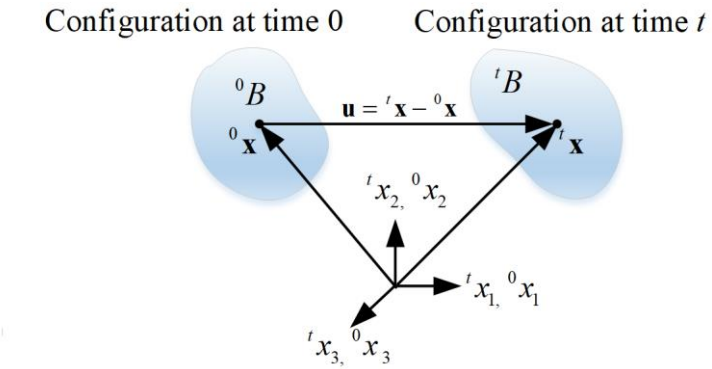

Figure 1. The finite deformation of a body [72] (The shape and position of a solid body before and after deformation.).

In order to describe the different behaviors of shear and bulk, the deformation usually splits into the deviatoric part and the volumetric part [72]. Accordingly, a multiplicative decomposition of the deformation gradient tensor ${}^t\mathbf{F}$ is performed:

$$ {}^t\mathbf{F} = {}^t\mathbf{F}_{\mathrm{d}} \, {}^t\mathbf{F}_{\mathrm{v}}, \tag{1} $$

where ${}^t\mathbf{F}_{\mathrm{d}}$ and ${}^t\mathbf{F}_{\mathrm{v}}$ are, respectively, the deviatoric and volumetric components of

${}^t\mathbf{F}$, and defined by

$$ {}^t\mathbf{F}_{\mathrm{d}} = (\det[{}^t\mathbf{F}])^{-1/3}\,{}^t\mathbf{F}\,, \quad {}^t\mathbf{F}_{\mathrm{v}} = (\det[{}^t\mathbf{F}])^{1/3}\mathbf{I}_2\,, \tag{2} $$

in which $\mathbf{I}_2$ is the second-order identity tensor. Thus, the associated modified right Cauchy–Green tensor ${}^t\bar{\mathbf{C}}$ and the modified Green strain tensor ${}^t\bar{\mathbf{E}}$ can be written as

$$ {}^t\bar{\mathbf{C}} = {}^t\mathbf{F}_{\mathrm{d}}{}^{\mathrm{T}}\,{}^t\mathbf{F}_{\mathrm{d}}, \quad {}^t\bar{\mathbf{E}} = \frac{1}{2}({}^t\bar{\mathbf{C}} - \mathbf{I}_2)\,. \tag{3} $$

2.2 Anisotropic hyperelastic material model

Biological soft tissues are almost always modeled as anisotropic hyperelastic materials because of their highly anisotropic and nonlinear elastic behaviors. Two different descriptions, strain-based and invariant-based, are often used to represent the strain energy potential of the anisotropic hyperelastic materials. In this paper, a strain-based phenomenological constitutive model, the Fung-type strain-energy function [8], which exhibits great capability in describing many biological soft tissues, is considered.

Most biological soft tissues are compressible due to their high-water content and low permeability. In a pure displacement-based element, the incompressibility condition is usually treated by using a penalty term [73] to prevent numerical instabilities of the iterative solution strategy, and it does not require any additional computational effort.

A generalized decoupled 3D Fung-type strain-energy function that is also used in Abaqus [13] is given by:

$$ \psi = \psi_{\mathrm{iso}} + \psi_{\mathrm{vol}} \quad , \tag{4} $$

$$ \psi_{\mathrm{iso}} = \frac{c}{2}\left(e^{Q} - 1\right), \tag{5} $$

$$\psi_{\text{vol}} = \frac{1}{D}\left(\frac{\left({}^{t}J\right)^{2} - 1}{2} - \ln {}^{t}J \right), \tag{6}$$

where ψ is the strain energy per unit of the reference volume; ψ_{vol} the purely volumetric contribution which is also considered as a penalty function; ψ_{iso} the purely isochoric contribution to the free energy; c a material parameter; e the natural logarithm; ${}^{t}J = \det[{}^{t}\mathbf{F}]$ the volume ratio; and D the penalty factor for incompressibility condition, typically set to be 1×10^{-6} or less to keep a good balance between the incompressibility condition and the convergence of the Newton–Raphson scheme [74]. In the above formulation, Q is given by

$$Q = {}^{t}\bar{\mathbf{E}} : \mathbf{b} : {}^{t}\bar{\mathbf{E}} = {}^{t}\bar{E}_{ij} b_{ijkl} {}^{t}\bar{E}_{kl}, \tag{7}$$

where b_{ijkl} are the dimensionless symmetric fourth-order tensor of anisotropic material constants and ${}^{t}\bar{E}_{ij}$ are the components of the modified Green strain tensor.

2.3 Hyperelastic stress response

The strain-energy function ψ given by Equation (4) can be treated as a function of the modified Green strain tensor ${}^{t}\bar{\mathbf{E}}$. Then, the second Piola–Kirchhoff stress tensor ${}^{t}\mathbf{S}$ can be written as [72]:

$${}^{t}\mathbf{S} = \frac{\partial \psi({}^{t}\bar{\mathbf{E}})}{\partial {}^{t}\mathbf{E}}, \tag{8}$$

with

$$\frac{\partial {}^{t}J}{\partial {}^{t}\mathbf{E}} = {}^{t}J\, {}^{t}\mathbf{C}^{-1} \quad \text{and} \quad \frac{\partial {}^{t}\bar{\mathbf{E}}}{\partial {}^{t}\mathbf{E}} = {}^{t}J^{-2/3}\left(\mathbf{I}_4 - \frac{1}{3}\, {}^{t}\bar{\mathbf{C}} \otimes {}^{t}\bar{\mathbf{C}}^{-1} \right), \tag{9}$$

where ${}^{t}\mathbf{E}$ is the Green strain tensor, ${}^{t}\mathbf{C}$ the right Cauchy–Green tensor, and $\mathbf{I}_4$ the fourth-order identity tensor.

The Cauchy stress tensor ${}^{t}\boldsymbol{\sigma}$ is expressed as

$$ {}^{t}\boldsymbol{\sigma}={}^{t}J^{-1}\,{}^{t}\mathbf{F}\cdot{}^{t}\mathbf{S}\cdot{}^{t}\mathbf{F}^{\mathrm{T}}. \tag{10}$$

3. The unsymmetric element US-ATFH8 for finite deformation

This section describes the construction of the element US-ATFH8. Sub-section 3.1 explains how the analytical trial functions are used to interpolate the incremental displacement field. Sub-section 3.2 describes the consistent tangent modulus which is used to update the analytical trial functions in each incremental step. A specially designed algorithm is presented in sub-section 3.3 to update the deformation gradient in each incremental step. After deriving the internal force vector in sub-section 3.4, the finite element equilibrium equation is obtained and consistently linearized, which results in the final tangent stiffness matrix (sub-section 3.5).

3.1 The analytical trial functions (ATFs) interpolation for incremental displacement field

The ATFs derived from the governing equations for linear elasticity can effectively improve the approximation accuracy in each increment of finite deformation analysis [61, 62]. They are adopted to interpolate the incremental displacement fields $\{\Delta\mathbf{u}\}$, which are used for computing the Cauchy stress.

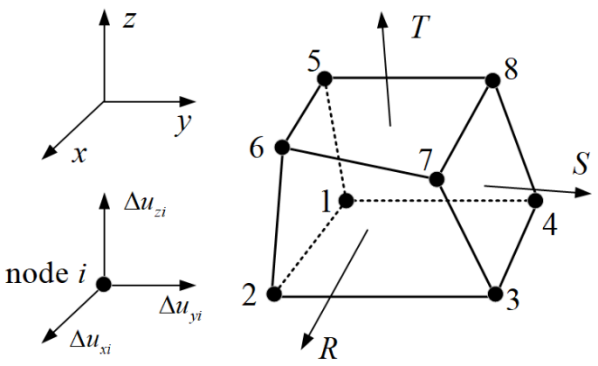

Figure 2. An 8-node hexahedral solid element.

An 8-node, 24-DOF hexahedral solid element is shown in **Figure 2**. Its incremental displacement fields $\{\Delta\mathbf{u}\}$ from time t to $t+\Delta t$ are interpolated as follows [62]:

$$\{\Delta\mathbf{u}\}=\begin{Bmatrix}\Delta u_x\\ \Delta u_y\\ \Delta u_z\end{Bmatrix}=[\mathbf{P}]\{\boldsymbol{\alpha}\}, \tag{11}$$

$$[\mathbf{P}]=\left[\begin{array}{ccccccccccc:ccc:ccc}1&0&0&{}^{t_h}R&0&0&{}^{t_h}S&0&0&{}^{t_h}T&0&0&{}^{t_h}U_{13}&\cdots&{}^{t_h}U_{21}&{}^{t_h}f&0&0\\0&1&0&0&{}^{t_h}R&0&0&{}^{t_h}S&0&0&{}^{t_h}T&0&{}^{t_h}V_{13}&\cdots&{}^{t_h}V_{21}&0&{}^{t_h}f&0\\0&0&1&0&0&{}^{t_h}R&0&0&{}^{t_h}S&0&0&{}^{t_h}T&{}^{t_h}W_{13}&\cdots&{}^{t_h}W_{21}&0&0&{}^{t_h}f\end{array}\right], \tag{12}$$

$${}^{t_h}f={}^{t_h}R\,{}^{t_h}S\,{}^{t_h}T$$

$$\{\boldsymbol{\alpha}\}=\begin{bmatrix}\alpha_1 & \cdots & \alpha_{24}\end{bmatrix}^{\mathrm{T}}, \tag{13}$$

where $\left({}^{t_h}R,{}^{t_h}S,{}^{t_h}T\right)$ are the skew coordinates [60] (see Appendix A) at time $t_h=t+\Delta t/2$, $\left({}^{t_h}U_j,{}^{t_h}V_j,{}^{t_h}W_j\right)$ the quadratic displacement solutions in terms of the skew coordinate at time t_h, which depend on both the configuration and the material parameters (see Appendix B), and α_k (k=1~24) are 24 undetermined coefficients.

Substitution of the nodal coordinates and incremental nodal displacements into Equation (11) yields:

$$\{\Delta\mathbf{u}\}=\left[{}^{t_h}\mathbf{N}\right]\{\Delta\mathbf{q}^e\}, \tag{14}$$

$$\left[{}^{t_h}\mathbf{N}\right]=\begin{bmatrix}{}^{t_h}N_{x1} & {}^{t_h}N_{x2} & {}^{t_h}N_{x3} & \cdots & {}^{t_h}N_{x22} & {}^{t_h}N_{x23} & {}^{t_h}N_{x24}\\ {}^{t_h}N_{y1} & {}^{t_h}N_{y2} & {}^{t_h}N_{y3} & \cdots & {}^{t_h}N_{y22} & {}^{t_h}N_{y23} & {}^{t_h}N_{y24}\\ {}^{t_h}N_{z1} & {}^{t_h}N_{z2} & {}^{t_h}N_{z3} & \cdots & {}^{t_h}N_{z22} & {}^{t_h}N_{z23} & {}^{t_h}N_{z24}\end{bmatrix}, \tag{15}$$

$$\{\Delta\mathbf{q}^e\}=\begin{bmatrix}\Delta u_{x1} & \Delta u_{y1} & \Delta u_{z1} & \cdots & \Delta u_{x8} & \Delta u_{y8} & \Delta u_{z8}\end{bmatrix}^{\mathrm{T}}, \tag{16}$$

where $\{\Delta\mathbf{q}^e\}$ is the nodal incremental displacement vector, and $\left[{}^{t_h}\mathbf{N}\right]$ the shape function matrix formulated by composite coordinate interpolation. For an anisotropic hyperelastic material, $\left[{}^{t_h}\mathbf{N}\right]$ is a function of consistent tangent modulus ${}^{t_h}\mathbf{C}$ (Note:

it is different from the spatial tangent moduli adopted in reference [39]) and the spatial coordinates ${}^{t_h}\mathbf{x}$,

$$\left[{}^{t_h}\hat{\mathbf{N}}\right]=\left[{}^{t_h}\hat{\mathbf{N}}\left({}^{t_h}\mathbf{x},\ {}^{t_h}\mathbf{C}\right)\right]. \tag{17}$$

3.2 Consistent tangent modulus for general anisotropic hyperelastic materials

It should be noted that the ATFs cannot be used to interpolate the total displacement fields, and they are valid only in each increment of finite deformation. This means that a relationship between the strain increments and the Cauchy stress increments is needed. The strain increments are defined by the symmetric part of the displacement increment gradient.

Different numerical approximations for the tangent modulus of anisotropic hyperelastic material have been suggested [75, 76]. In this paper, the consistent tangent modulus is defined as:

$${}^{t}\mathbf{C}=\frac{1}{{}^{t}J}\frac{\partial\Delta({}^{t}J\,{}^{t}\boldsymbol{\sigma})}{\partial\Delta\,{}^{t}\boldsymbol{\varepsilon}}, \tag{18}$$

and it has the same form as the material Jacobian matrix used in the user subroutine UMAT for Abaqus [13]. For a small increment with nearly incompressible deformation, the relationships between the incremental strain and the incremental Cauchy stress vectors are assumed to be linear:

$$\left\{\Delta\,{}^{t}\boldsymbol{\sigma}\right\}=\left[{}^{t}\mathbf{C}\right]\left\{\Delta\,{}^{t}\boldsymbol{\varepsilon}\right\}, \tag{19}$$

$$\left\{\Delta\,{}^{t}\boldsymbol{\varepsilon}\right\}=\left[{}^{t}\mathbf{C}\right]^{-1}\left\{\Delta\,{}^{t}\boldsymbol{\sigma}\right\}. \tag{20}$$

For the total-form constitutive laws, the tensor components of the consistent tangent modulus ${}^{t}\mathbf{C}$ are given by:

$$ {}^{t}\mathrm{C}_{ijkl} = \frac{1}{2}\,{}^{t}J^{-1}\left({}^{t}F_{lm}\frac{\partial\left({}^{t}J\,{}^{t}\sigma_{ij}\right)}{\partial\,{}^{t}F_{km}} + {}^{t}F_{km}\frac{\partial\left({}^{t}J\,{}^{t}\sigma_{ij}\right)}{\partial\,{}^{t}F_{lm}} \right). \tag{21} $$

Because of the major and minor symmetries of the consistent tangent modulus ${}^{t}\mathbf{C}$, associated tangent moduli matrix notation $\left[{}^{t}\mathbf{C}\right]$ can be readily obtained. Numerical tests in Section 4 will show that the use of ATFs with consistent tangent modulus can ensure the rapid convergence for the suggested formulation.

3.3 The stress computation and update of the deformation gradient

For hyperelastic material, the Cauchy stress can be directly calculated from a total-form constitutive equation relating to the deformation gradient:

$$ \left\{{}^{t+\Delta t}\boldsymbol{\sigma}\right\} = \left\{{}^{t+\Delta t}\boldsymbol{\sigma}({}^{t+\Delta t}\mathbf{F})\right\}. \tag{22} $$

The incremental deformation gradient matrix from time t to $t+\Delta t$ is defined as

$$ \left[{}^{t+\Delta t}\Delta\mathbf{F}\right] = \frac{\partial\left\{{}^{t+\Delta t}\mathbf{x}\right\}}{\partial\left\{{}^{t}\mathbf{x}\right\}} = \left[\mathbf{I}_2\right] + \left[\frac{\partial\left\{\Delta\mathbf{u}\right\}}{\partial\left\{{}^{t}\mathbf{x}\right\}}\right], \tag{23} $$

where $\left[\mathbf{I}_2\right]$ is the second-order identity matrix.

The deformation gradient at time $t+\Delta t$ is calculated by multiplying the incremental deformation gradient by the deformation gradient at time t:

$$ \left[{}^{t+\Delta t}\mathbf{F}\right] = \left[{}^{t+\Delta t}\Delta\mathbf{F}\right]\left[{}^{t}\mathbf{F}\right]. \tag{24} $$

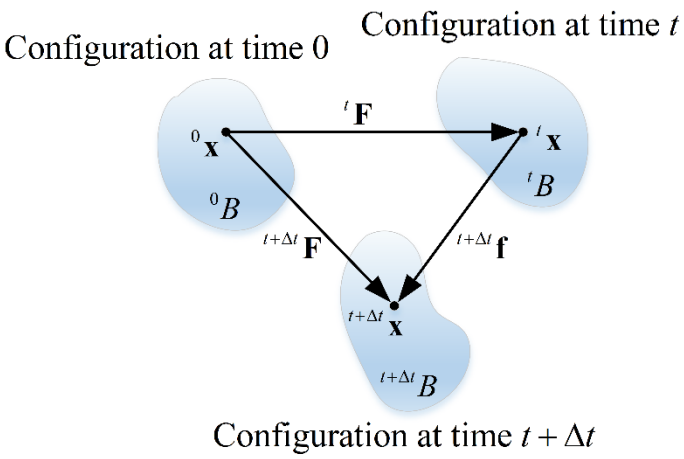

Figure 3. The update of deformation gradient during the finite deformation of a body. (The deformation gradient at time $t+\Delta t$ is obtained by multiplying the incremental deformation gradient by the deformation gradient at time t.)

The deformation process from configuration ${}^{t}B$ to ${}^{t+\Delta t}B$ is regarded as linear, which means that

$$ {}^{t_h}\mathbf{x} = \left({}^{t}\mathbf{x} + {}^{t+\Delta t}\mathbf{x} \right) / 2 = {}^{t}\mathbf{x} + \Delta\mathbf{u} / 2 . \tag{25} $$

Substitution of Equations (14), (17) and (25) into Equation (23) yields

$$ \left[{}^{t+\Delta t}\Delta\mathbf{F} \right] = \left[\mathbf{I} \right] + \left[\frac{\partial \left\{ \Delta\mathbf{u} \right\}}{\partial \left\{ {}^{t_h}\mathbf{x} \right\}} \right] \left[\mathbf{I} - \frac{1}{2} \frac{\partial \left\{ \Delta\mathbf{u} \right\}}{\partial \left\{ {}^{t_h}\mathbf{x} \right\}} \right]^{-1} . \tag{26} $$

The Cauchy stress $\left\{ {}^{t+\Delta t}\boldsymbol{\sigma} \right\}$ in the current configuration ${}^{t+\Delta t}B$ is obtained by substituting Equations (24) and (26) into Equation (22). Hence, the Cauchy stress is successfully acquired through the incremental displacement fields interpolated by ATFs.

3.4 Internal force vector

For the spatial configuration, the element internal force vector is given by

$$ \left\{ {}^{t}\mathbf{f}_{\text{int}}^{e} \right\} = \int_{{}^{t}B} \left[{}^{t}\bar{\mathbf{B}}_{L} \right]^{\mathrm{T}} \left\{ \hat{\boldsymbol{\sigma}}({}^{t}\mathbf{F}) \right\} \mathrm{d}\,{}^{t}V , \tag{27} $$

where $\left\{ \hat{\boldsymbol{\sigma}}({}^{t}\mathbf{F}) \right\}$ is the Voigt form of the Cauchy stress tensor, and for a hyperelastic constitutive model, it is the function of the deformation gradient ${}^{t}\mathbf{F}$; $\left[{}^{t}\bar{\mathbf{B}}_{L} \right]$ is the

discrete spatial symmetric gradient operator matrix, and has the similar form to the linear strain-displacement matrix, in which the derivatives of the shape functions are derived with respect to the spatial coordinates of the finite element mesh, i.e., at the deformed configuration defined at time t:

$$\left[{}^{t}\bar{\mathbf{B}}_{L}\right]=\begin{bmatrix} \bar{N}_{1,{}^{t}x} & 0 & 0 & \cdots & \bar{N}_{8,{}^{t}x} & 0 & 0 \\ 0 & \bar{N}_{1,{}^{t}y} & 0 & \cdots & 0 & \bar{N}_{8,{}^{t}y} & 0 \\ 0 & 0 & \bar{N}_{1,{}^{t}z} & \cdots & 0 & 0 & \bar{N}_{8,{}^{t}z} \\ \bar{N}_{1,{}^{t}y} & \bar{N}_{1,{}^{t}x} & 0 & \cdots & \bar{N}_{8,{}^{t}y} & \bar{N}_{8,{}^{t}x} & 0 \\ 0 & \bar{N}_{1,{}^{t}z} & \bar{N}_{1,{}^{t}y} & \cdots & 0 & \bar{N}_{8,{}^{t}z} & \bar{N}_{8,{}^{t}y} \\ \bar{N}_{1,{}^{t}z} & 0 & \bar{N}_{1,{}^{t}x} & \cdots & \bar{N}_{8,{}^{t}z} & 0 & \bar{N}_{8,{}^{t}x} \end{bmatrix}, \tag{28}$$

with

$$\bar{N}_{I}=\frac{1}{8}(1+\xi_{I}\xi)(1+\eta_{I}\eta)(1+\zeta_{I}\zeta) \qquad I=(1,2,...,8)\,. \tag{29}$$

where (ξ_I,η_I,ζ_I) are the nodal isoparametric coordinates.

For the unsymmetric element US-ATFH8 [53], two different sets of interpolation functions are simultaneously used. The first set employs the shape functions of the conventional 8-node trilinear isoparametric element to formulate the matrix $\left[{}^{t}\bar{\mathbf{B}}_{L}\right]$. The second set adopts the skew coordinate interpolation scheme with the ATFs and has been given by Equation (15). It is used to construct the incremental displacement fields $\{\Delta\mathbf{u}\}$ for calculating the incremental deformation gradient $\left[{}^{t+\Delta t}\Delta\mathbf{F}\right]$.

A 2×2×2 Gauss integration scheme is used to evaluate the internal force vector given by Equation (27)

$$\begin{aligned}\left\{{}^{t}\mathbf{f}_{\text{int}}^{e}\right\} &= \int_{{}^{t}B}\left[{}^{t}\overline{\mathbf{B}}_{L}\right]^{\mathrm{T}}\left\{{}^{t}\hat{\boldsymbol{\sigma}}\right\}\mathrm{d}\,{}^{t}V \\ &= \int_{-1}^{1}\int_{-1}^{1}\int_{-1}^{1}\frac{\left[{}^{t}\overline{\mathbf{B}}_{L}^{*}\right]^{\mathrm{T}}}{|\mathbf{J}|}\left\{{}^{t}\hat{\boldsymbol{\sigma}}\right\}|\mathbf{J}|\,\mathrm{d}\xi\mathrm{d}\eta\mathrm{d}\zeta \\ &= \int_{-1}^{1}\int_{-1}^{1}\int_{-1}^{1}\left[{}^{t}\overline{\mathbf{B}}_{L}^{*}\right]^{\mathrm{T}}\left\{{}^{t}\hat{\boldsymbol{\sigma}}\right\}\mathrm{d}\xi\mathrm{d}\eta\mathrm{d}\zeta\end{aligned} \quad . \tag{30}$$

It can be observed that the Jacobian determinant in matrix $\left[{}^{t}\overline{\mathbf{B}}_{L}\right]$ and the Jacobian determinant produced by the Gaussian integral are cancelled exactly. Moreover, the relationship between the skew coordinates and the Cartesian coordinates is always linear. This means that no Jacobian determinant exists in the denominator of the integral, so that the resulting model will avoid issues caused by the ill-conditioned shape and be insensitive to mesh distortion.

3.5 The finite element equilibrium equation and consistent linearization.

The equilibrium conditions at time $t+\Delta t$ can be expressed as:

$$\left\{{}^{t+\Delta t}\mathbf{f}_{\text{int}}\right\}-\left\{{}^{t+\Delta t}\mathbf{f}_{\text{ext}}\right\}=\left\{\mathbf{0}\right\}, \tag{31}$$

where $\left\{{}^{t+\Delta t}\mathbf{f}_{\text{int}}\right\}$ and $\left\{{}^{t+\Delta t}\mathbf{f}_{\text{ext}}\right\}$ are the internal and external nodal force vectors, respectively.

The most common scheme for the iterative solution of systems of a nonlinear algebraic equation is the Newton–Raphson algorithm. The residual vector is written as

$$\left\{{}^{t+\Delta t}\mathbf{R}({}^{t+\Delta t}\mathbf{q})\right\}:=\left\{{}^{t+\Delta t}\mathbf{f}_{\text{int}}({}^{t+\Delta t}\mathbf{q})\right\}-\left\{{}^{t+\Delta t}\mathbf{f}_{\text{ext}}\right\}=\left\{\mathbf{0}\right\}, \tag{32}$$

where ${}^{t+\Delta t}\mathbf{q}$ is the vector of nodal displacements corresponding to time $t+\Delta t$.

During a typical Newton-Raphson iteration *k*, the following linear system is solved for the increment of displacement $\left\{\Delta\mathbf{q}^{(k)}\right\}$:

$$\left[{}^{t}\mathbf{K}_{T}\left({}^{t}\mathbf{q}^{(k)}\right)\right]\left\{\Delta\mathbf{q}^{(k)}\right\}=\left\{{}^{t+\Delta t}\mathbf{f}_{\text{ext}}\right\}-\left\{{}^{t}\mathbf{f}_{\text{int}}\left({}^{t}\mathbf{q}^{(k)}\right)\right\}. \tag{33}$$

The total internal force vector and the total tangent stiffness matrix are obtained by a standard finite element assembly procedure from the element internal force and the element tangent stiffness.

The tangent stiffness matrix of any element can be obtained by direct differentiation:

$$\left[{}^{t}\mathbf{K}_{T}^{e} \right] = \frac{\partial \left(\left\{ {}^{t+\Delta t}\mathbf{f}_{\text{ext}}^{e} \right\} - \left\{ {}^{t}\mathbf{f}_{\text{int}}^{e} \right\} \right)}{\partial \left\{ {}^{t}\mathbf{q}^{e} \right\}}, \tag{34}$$

where $\left\{ {}^{t}\mathbf{q}^{e} \right\}$ is the vector of nodal displacements corresponding to time t.

In this paper, the derivation of the tangent stiffness matrix, Equation (34), is performed with the help of the automatic differentiation program Acegen developed by Korelc [77]. Since the two different sets of interpolation functions are used, the tangent stiffness is generally unsymmetric and, therefore, requires an unsymmetric solver in finite element computations.

4. **Numerical examples**

In this section, two single-element tests, four common benchmarks, and three cardiac examples are presented to illustrated the performance of the proposed formulation US-ATFH8. For all these numerical examples, the nearly-incompressible generalized decoupled three-dimensional Fung-type anisotropic constitutive law is adopted, and the associated material parameters are given in Appendix C.

The results obtained by two Abaqus 8-node hexahedral solid elements are given for comparisons in examples 1~6 and example 9: (i) C3D8H (8-node linear element, hybrid with constant pressure); (ii) C3D8IH (8-node linear element, 9 incompatible

modes, hybrid with linear pressure).

The simulations with the formulation US-ATFH8 for hyperelastic finite deformation are implemented by the user element subroutine of Abaqus [13]. All terms of the element formulation are evaluated by using the 2×2×2 Gaussian integration scheme. The incremental-iterative Newton-Raphson scheme is selected to solve these nonlinear problems. The default convergence criteria set by Abaqus were kept unchanged for all simulations. Automatic incrementation control is specified, because Abaqus can automatically adjust the size of the increments to solve the nonlinear problem efficiently.

4.1 Single element test

In order to verify the correctness of the derived equations and the implementation, numerical tests with analytical solutions were performed on single element.

4.1.1 The selection of the penalty factor

In this section, the selection of the value of D in penalty function is discussed by comparing the results for different values. As shown in **Figure 4(a)**, a 1mm × 1mm × 1mm isotropic cube is meshed as a single finite element. A simple tension was studied with the different values of D. For simple tension along the x-direction, the deformation gradient tensor for incompressiobility can be given as:

$$\mathbf{F}=\begin{bmatrix}\lambda_x & 0 & 0\\ 0 & \lambda_y & 0\\ 0 & 0 & \lambda_z\end{bmatrix}=\begin{bmatrix}\lambda & 0 & 0\\ 0 & 1/\sqrt{\lambda} & 0\\ 0 & 0 & 1/\sqrt{\lambda}\end{bmatrix} \tag{35}$$

Different values of D were tested, and the numerical results are shown in **Figure 5**. It

can be observed that the incompressibility is enforced with the decrease of D. When D is less than 1×10^{-6}, the nearly-incompressible condition is reached. When D equals to zero, the incompressibility is fully enforced. However, the extremely small value of D makes the system matrix ill-conditioned, which leads to numerical problems. Because the myocardium is not truly incompressible, the reasonable selection of the value of D can provide a good approximation for incompressibility.

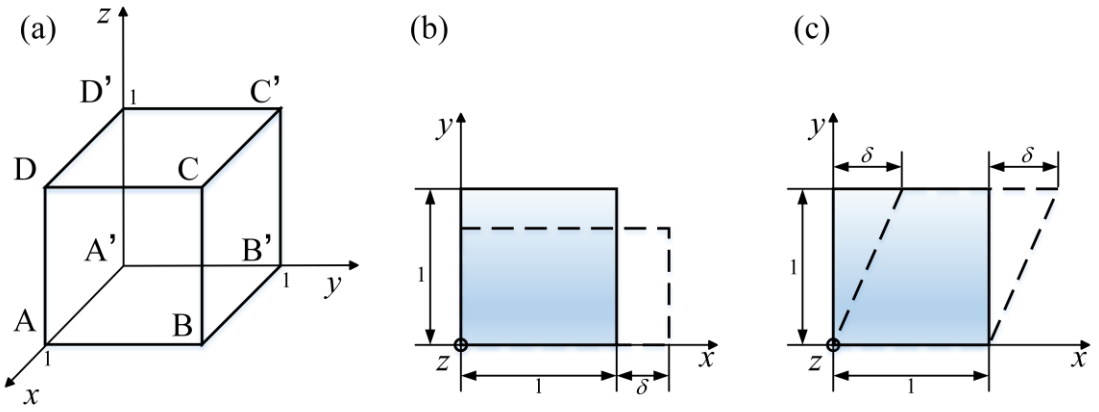

Figure 4. Deformation of a single element. (a) A 1mm × 1mm × 1mm cube is meshed as a single finite element. (b) Uniaxial tension of a nearly-incompressible anisotropic hyperelastic soft cube. (c) Simple shear of a nearly-incompressible anisotropic hyperelastic soft cube.

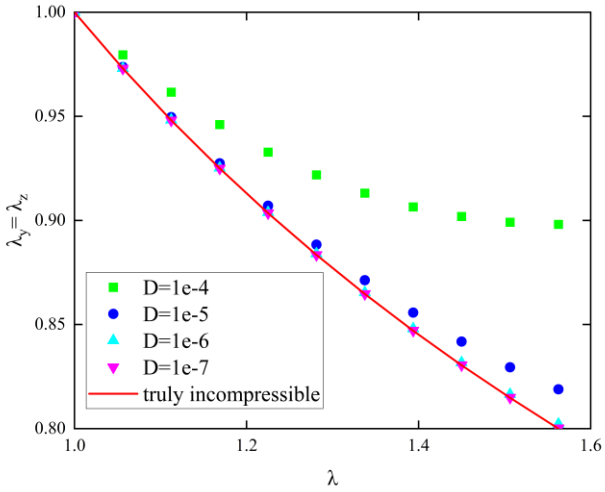

Figure 5. The comparison of the results of simple tension with different penalty factor

D with the ground truth of truly incompressible state.

4.1.2 Uniaxial tension of an anisotropic nearly-incompressible hyperelastic soft cube

As shown in **Figure 4(a)**, a 1mm × 1mm × 1mm cube is meshed as a single finite element. The deformation process of uniaxial tension is depicted in **Figure 4(b)**. The boundary conditions are: i) for x=0, the displacement u_1=0; ii) for y=0, the displacement u_2=0; iii) for z=0, the displacement u_3=0; iv) for x=1mm (face ABCD), the displacement $u_1 = \delta$ mm. The σ_{11}-δ curves are plotted in **Figure 6(a)**. The results obtained by elements US-ATFH8, C3D8H, and C3D8IH all agree well with the analytical solutions.

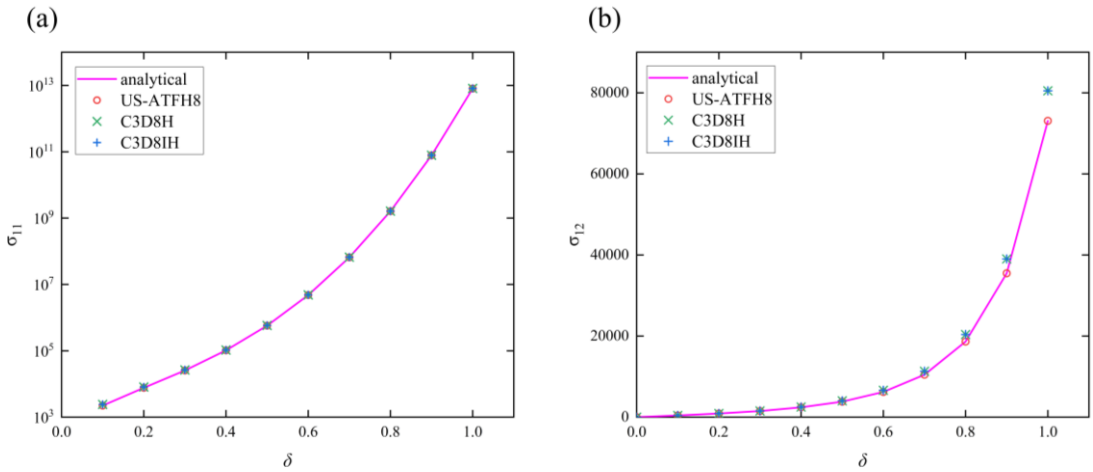

Figure 6. One element test. (a) Comparison of analytical and numerical results of the soft cube under uniaxial tension. (b) Comparison of analytical and numerical results of the soft cube under simple shear.

4.1.3 Simple shear of an anisotropic nearly-incompressible hyperelastic soft cube

For the cube defined in the last example, the deformation process of simple shear is depicted in **Figure 4(c)**. The boundary conditions are: i) for y=0, the displacements u_1=u_2=u_3=0; ii) for y=1 (face BCC'B'), the displacements u_2 =u_3=0, $u_1 = \delta$ mm. The σ_{12}-δ curves are plotted in **Figure 6(b)**. Again, the results obtained by element US-

ATFH8 agree very well with the analytical solutions, and are much better than those obtained by elements C3D8H and C3D8IH, whose errors increase slightly with the increase of shear deformation.

4.2 Bending test for an orthotropic nearly-incompressible hyperelastic soft Cook's beam

An orthotropic nearly-incompressible hyperelastic soft Cook's beam is adopted to test the bending performance of the element US-ATFH8 for anisotropic hyperelasticity. The geometries of the structure are given in **Figure 7(a)**, where the left end is clamped and a distributed load is acting on the right end. The regular meshes from coarse to fine are used to perform the calculations, while only one element is set in the thickness direction.

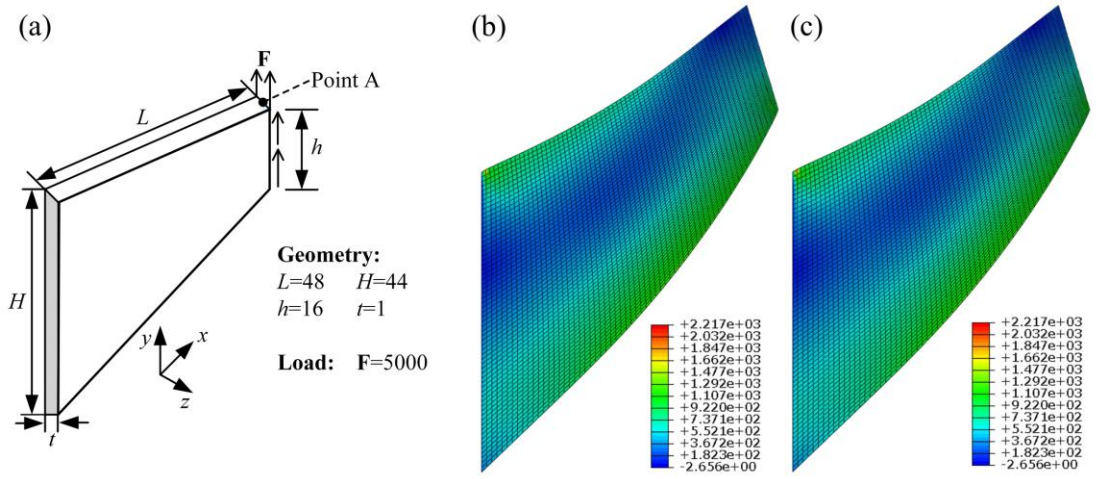

Figure 7. Soft Cook's beam. (a) Geometry and boundary conditions. (b) Mises stress on final deformed shapes with mesh 64 × 64 × 1 obtained by US-ATFH8. (c) Mises stress on final deformed shapes with mesh 64 × 64 × 1 obtained by C3D8IH.

The reference solution is obtained by element C3D8IH with a fine mesh (64×1×1). **Figure 7(b)** and **Figure 7(c)** give the contour plots of Mises stress on the deformed

configuration with the mesh 64×64×1 obtained by US-ATFH8 and C3D8IH. The convergence curves for point A obtained by US-ATFH8, C3D8H and C3D8IH are shown in **Figure 8**. It is observed that elements US-ATFH8, C3D8IH and C3D8H provide the same convergent solutions, but element US-ATFH8 exhibits the best convergence.

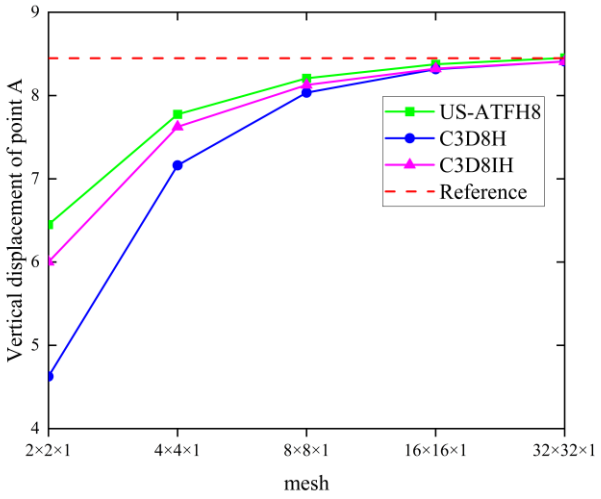

Figure 8. Convergence curves of the vertical displacement at point A of soft Cook's beam. The reference solution is obtained by element C3D8IH with a fine mesh (64×1×1).

4.3 Distortion tolerance test for an orthotropic nearly-incompressible hyperelastic soft cantilever beam

As shown in **Figure 9(a)**, an orthotropic cantilever beam is subjected to shear force on the right end while the left end is clamped. The detailed geometry and boundary conditions are given in **Figure 9(a)**. The convergence curves of vertical displacement of point A obtained by elements US-ATFH8, C3D8H and C3D8IH are given in **Figure 10**. The reference solution is obtained by element C3D8IH with a fine mesh (100×10×10). It can be observed that element US-ATFH8 possesses much better

convergence than element C3D8H, and element C3D8IH presents similar results to element US-ATFH8 because the regular meshes are used. The element C3D8H performs badly in this bending dominated problem because it is just a hybrid element with a constant pressure DOF based on the conventional trilinear element.

Then, several different distorted $20 \times 2 \times 2$ meshes are employed to test the performance of the elements. The distorted mode of mesh is shown in **Figure 9(b)**, in which δ denotes the distorted parameter. The vertical displacements of point A under different distorted meshes are given in **Table 1**. It can be seen that the performances of elements C3D8H and C3D8IH decrease quickly with the increase of the distorted parameter, while element US-ATFH8 can keep good precisions, which shows good mesh distortion tolerance.

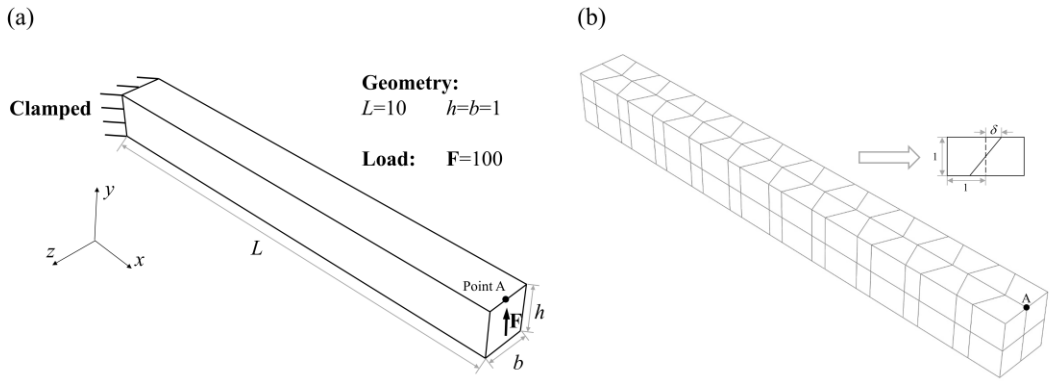

Figure 9. (a) Geometry and boundary conditions for soft cantilever beam. (b) Distorted mode of 20×2×2 meshes (δ denotes the distorted parameter).

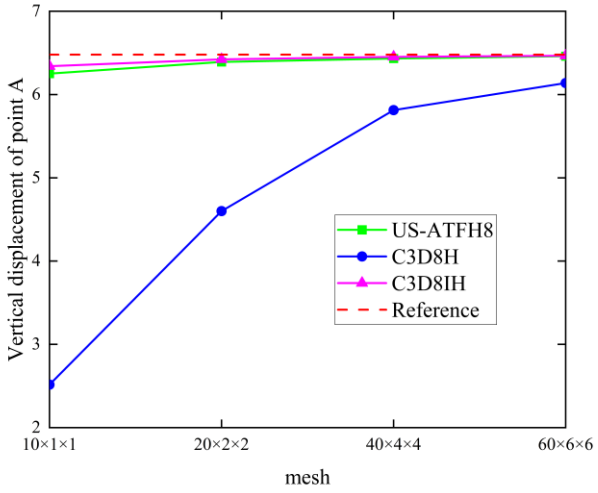

Figure 10. Convergence curves of the vertical displacement at point A of soft cantilever beam. The reference solution is obtained by element C3D8IH with a fine mesh (100×10×10).

Table 1. Vertical displacement results of point A using distorted meshes.

δ	Element type	V_A	error
0.06	C3D8H	4.31317	–33.4313%
	C3D8IH	5.90419	–8.8758%
	US-ATFH8	6.44517	–0.5264%
0.07	C3D8H	4.21731	–34.9108%
	C3D8IH	5.73178	–11.5368%
	US-ATFH8	6.44817	–0.4801%
0.08	C3D8H	4.11167	–36.5413%
	C3D8IH	5.54374	–14.4390%
	US-ATFH8	6.44970	–0.4565%
0.09	C3D8H	3.99804	–38.2950%
	C3D8IH	5.34455	–17.5132%
	US-ATFH8	6.45266	–0.4108%
0.1	C3D8H	3.87828	–40.1433%
	C3D8IH	5.13861	–20.6917%
	US-ATFH8	6.45450	–0.3824%
reference	C3D8IH (100×10×10 regular mesh)	6.47928	

4.4 Distortion tolerance test for a transversely-isotropic and nearly-incompressible hyperelastic soft curved beam

A transversely-isotropic curved beam subjected to a concentrated force is considered in this section. The details of geometry and boundary conditions are given in **Figure 11(a)**. Two ends of the curved beam are clamped and the concentrated force is loaded on the top. A regular 30×1×1 mesh and a distorted 30×1×1 mesh are adopted for calculation (**Figure 11(b)** and **Figure 11(c)**). The reference solution is obtained by element C3D8IH with a fine mesh (300×10×10).

The load-displacement curves of point A are plotted in **Figure 12** (It is worth noting that the results obtained by C3D8H is softer than the other two elements while it is always opposite in the isotropic problems. This is mainly due to the characters of the chosen anisotropic material), and the final deformed configuration obtained by element US-ATFH8 is given in **Figure 13**. It can be seen that no matter whether regular or distorted meshes are used, the present element US-ATFH8 can keep good precisions and is quite insensitive to mesh distortion, while the other two hybrid elements with additional degrees of freedom cannot achieve.

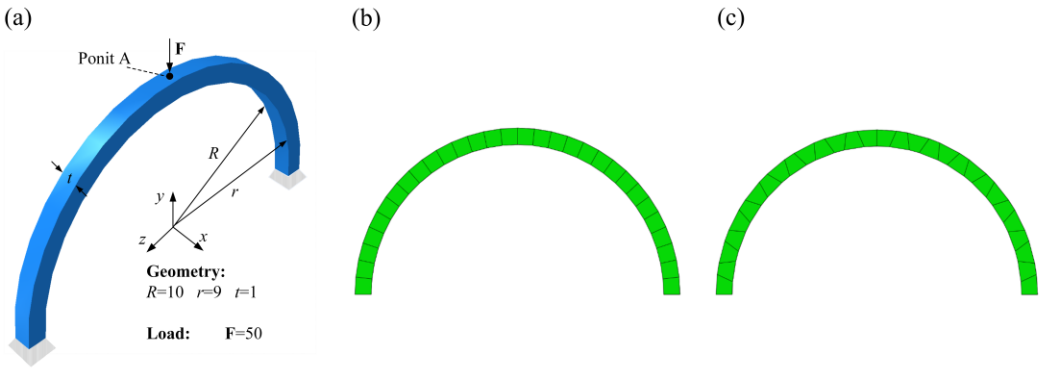

Figure 11. (a) Geometry and boundary conditions for soft curved beam. (b) Regular meshes for soft curved beam. (c) Distorted meshes for soft curved beam.

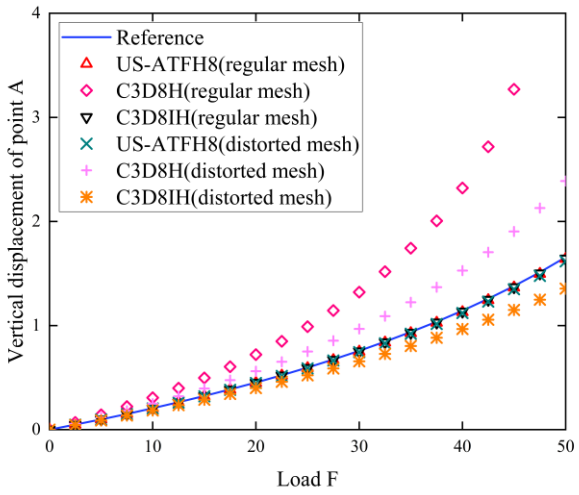

Figure 12. Load-deflection curves of point A of soft curved beam with regular mesh and distorted mesh. The reference solution is obtained by element C3D8IH with a fine mesh (300×10×10).

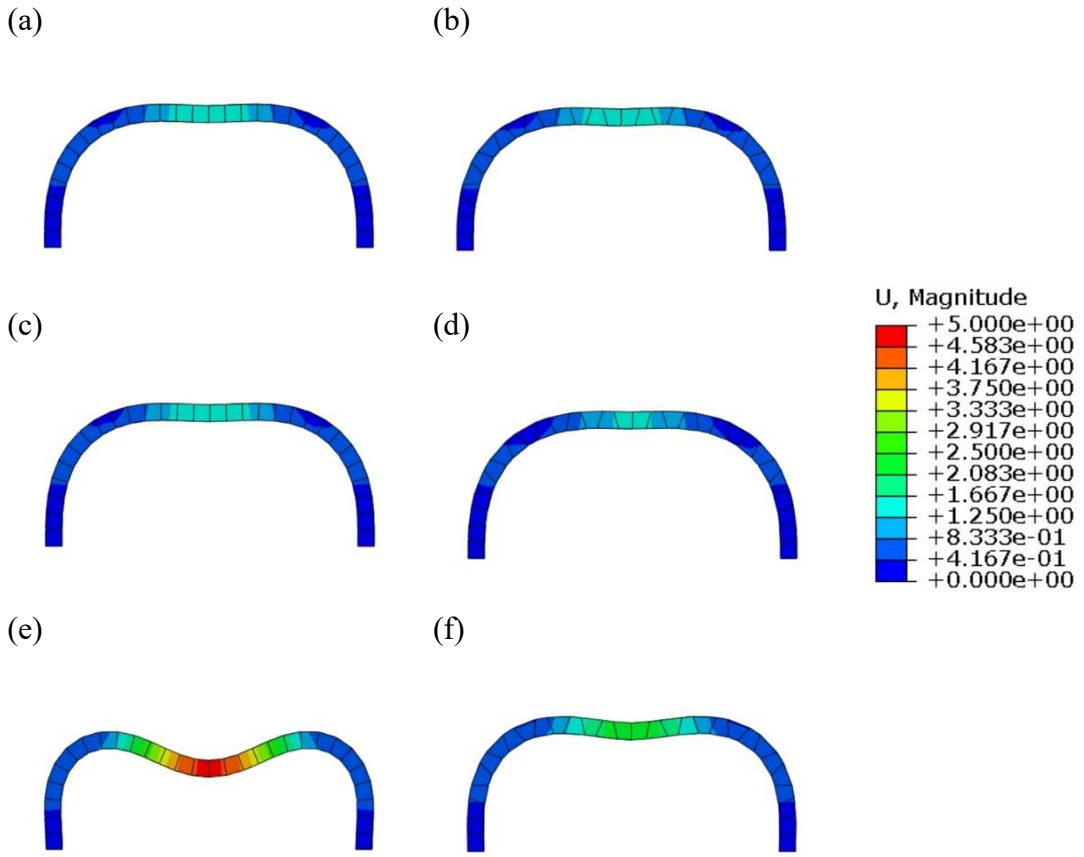

Figure 13. Final deformed shape with regular and distorted meshes for curved beam. (a) US-ATFH8 with regular mesh. (b) US-ATFH8 with distorted mesh. (c) C3D8IH with regular mesh. (d) C3D8IH with distorted mesh. (e) C3D8H with regular mesh. (f) C3D8H with distorted mesh.

4.5 Torsion of a transversely-isotropic hyperelastic soft beam with a square cross-section

As shown in **Figure 14(a)**, a transversely isotropic beam with a square cross-section is subjected to twisting load at its right free end and the left end is clamped. The detailed geometry and boundary conditions are given in **Figure 14(a)**. The purpose of this example is to study the mesh distortion tolerance of the present element. A maximum rotation of 2π is applied at the twisting face through multiple rotation increments. The deformed configurations of the twisting beam are given in **Figure 14(b)(c)(d).** The element US-ATFH8 completed the calculation successfully, while C3D8H and C3D8IH aborted before the rotation reaches π. The element US-ATFH8 shows good mesh distortion tolerance again in this twisting problem.

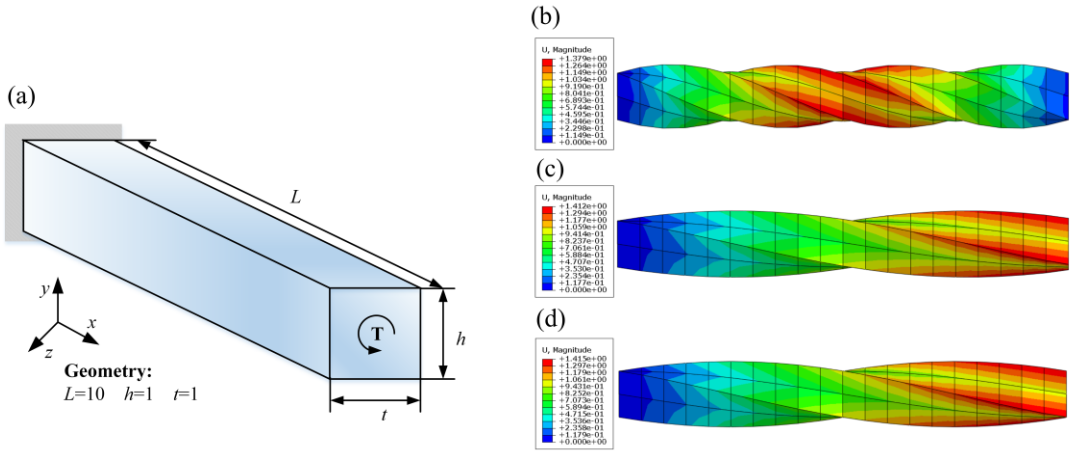

Figure 14. Torsion of a soft beam. (a) Geometry and boundary conditions for soft beam. (b) Element US-ATFH8 completed the calculation successfully. (c) Element C3D8H aborted at time step 0.4811. (d) Element C3D8IH aborted at time step 0.4983.

4.6 Benchmark test for a transversely-isotropic and nearly-incompressible hyperelastic soft beam

Land *et al* [14] introduced this benchmark of a cardiac beam, whose geometry and

boundary conditions are given in **Figure 15(a)**. This example tests the performance of a rectangular soft beam under pressure-type forces whose directions change with the deformed surface orientation. A transversely-isotropic constitutive law is adopted and the fiber direction is constant along the x-axis.

The maximum z-displacement was compared with several finite element solvers listed below in **Figure 15(b)** and the detailed description are available in reference [5] and the relative references therein.

(1) Cardioid: a hybrid 20-node hexahedral element with linear pressure DOFs (a 10-node hybrid tetrahedral element with linear pressure DOFs for example in section 4.7);

(2) CardioMechanics: a 10-node tetrahedral element;

(3) CARP: a 4-node hybrid tetrahedral element with constant pressure DOF;

(4) Elecmech: a hybrid 32-node hexahedral element with linear pressure DOFs;

(5) GlasgowHeart-IBFE: an immersed boundary method with 8-node hexahedral element;

(6) Hopkins-MESCAL: an 8-node hybrid hexahedral element with constant pressure DOF;

(7) LifeV: a 10-node tetrahedral element;

(8) MOOSE-EWE: a 20-node hybrid hexahedral element with linear pressure DOFs (a 10-node hybrid tetrahedral element with linear pressure DOFs for example in section 4.7);

(9) OpenCMISS: a 32-node hybrid hexahedral element with linear pressure DOFs;

(10) Simula-FEniCS: a 10-node hybrid tetrahedral element with linear pressure DOFs;

(11) PUC-FEAP: an 8-node hybrid hexahedral element with constant pressure DOF.

Element US-ATFH8 is a low-order element without any internal DOF and additional pressure DOF, but the element has a fast convergence speed and its final result is similar to those obtained by other hybrid elements and high-order elements.

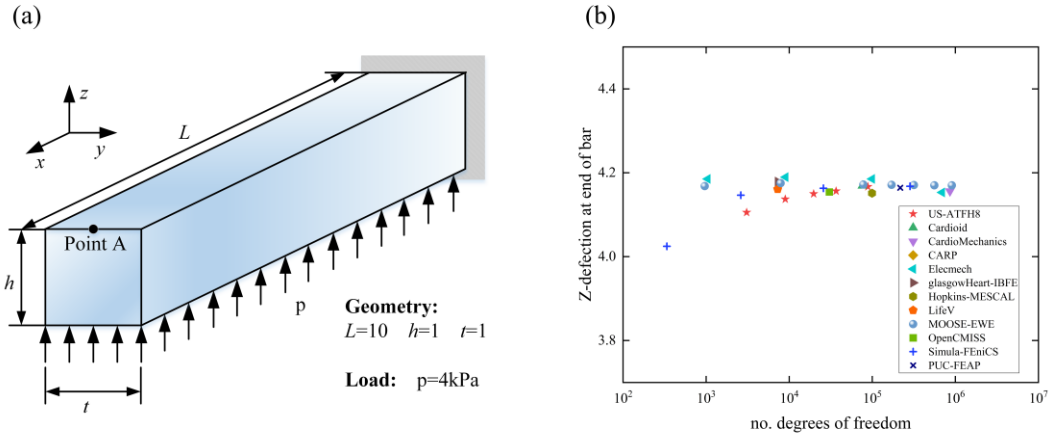

Figure 15. Soft beam benchmark. (a) Geometry and boundary conditions for soft beam. (b) The comparison of maximal deflection results at point A of the soft beam benchmark [14].

4.7 Passive inflation of an isotropic left ventricle model

The second benchmark was also introduced by Land *et al* [14], and it is an idealized ventricle characterized by an intersected set of ellipsoids, as shown in **Figure 16(a)**. The plane z=5mm is clamped in all directions and an inner pressure valued 10kPa is loaded on the endocardium.

The location of endocardial and epicardial apex points with respect to the number of degrees of freedom are given in **Figure 16(b)**, which are compared with the finite

element solvers described in section 4.7. The initial undeformed configurations and displacement contour on the final deformed configurations are shown in **Figure 17**. Compared to other specially designed elements, element US-ATFH8 presents fast convergence speed and similar convergence results, which proves its good performance again.

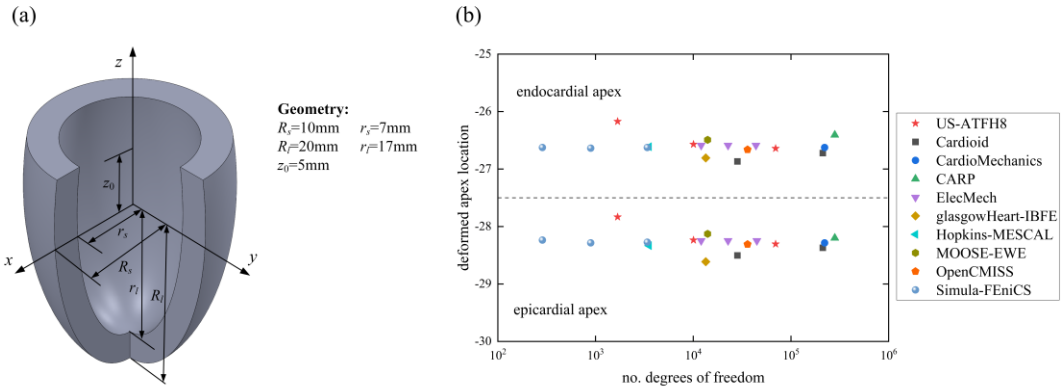

Figure 16. Idealized ventricle model. (a) Geometry conditions of idealized ventricle model. (b) The comparison of deformed locations of endocardial and epicardial apex points for US-ATFH8 and other elements [14].

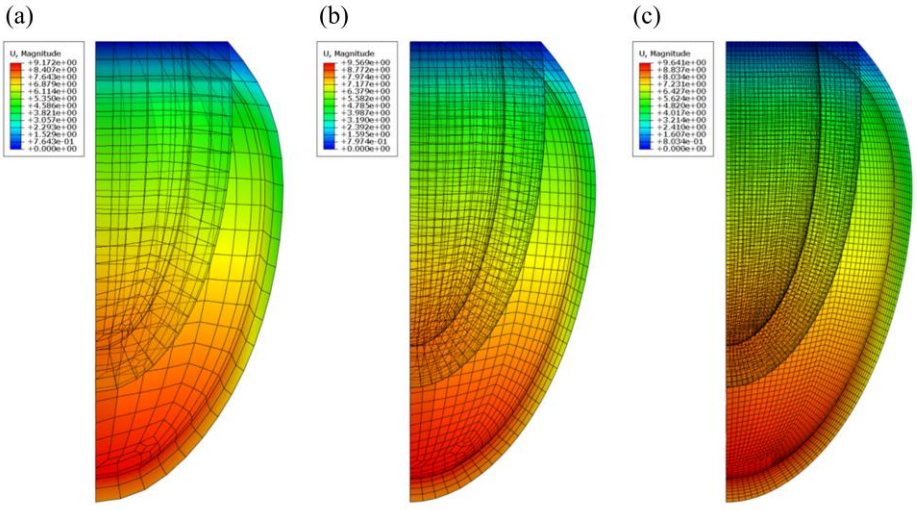

Figure 17. Initial undeformed configurations and displacement contour on the final deformed configurations of 1/4 ventricle obtained by US-ATFH8. (a) 1683 degrees of freedom. (b) 10062 degrees of freedom. (c) 69687 degrees of freedom.

4.8 Passive inflation of a fiber-reinforced left ventricle model

The final example considers the passive inflation of a fiber-reinforced left ventricle. The geometries and constrains are the same as the model in section 4.7. The orientations of fibers (**Figure 18(a)**) vary transmurally from the endocardial surface (45°) to the epicedial surface (-45°), and are generated using the LDRB method suggested by Bayer *et al* [78].

First, a 5kPa inner pressure is applied on the endocardial surface. The location of endocardial and epicardial apex points with respect to the load is given in **Figure 19(a)**. The results obtained by elements C3D8H and C3D8IH in Abaqus are also given for comparisons. It can be observed that element US-ATFH8 completed the calculation successfully, while C3D8H and C3D8IH aborted before the load reaching 5kPa.

Secondly, a 100kPa inner pressure is applied on the endocardial surface. The location of endocardial and epicardial apex points with respect to the load are given in **Figure 19(b)**, and the initial mesh and displacement contour on the final deformed configuration are given in **Figure 18(b)**. Furthermore, the initial shape and the final deformed shape of the element at the tip of the epicardial are given in **Figure 18(c)(d)**. It can be observed that this element also undergoes a heavily torsional deformation, and element US-ATFH8 keeps good mesh distortion tolerance all the time.

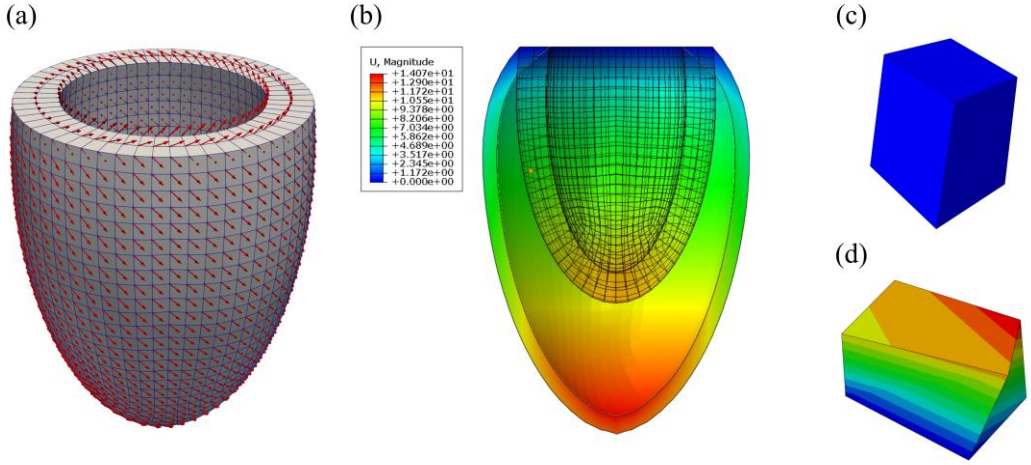

Figure 18. (a) Orientations of fibers in left ventricle model. (b) Initial mesh and displacement contour on final deformed configuration. (c) Initial shape of the element in the tip of epicardium. (d) Final deformed shape of the element in the tip of epicardium.

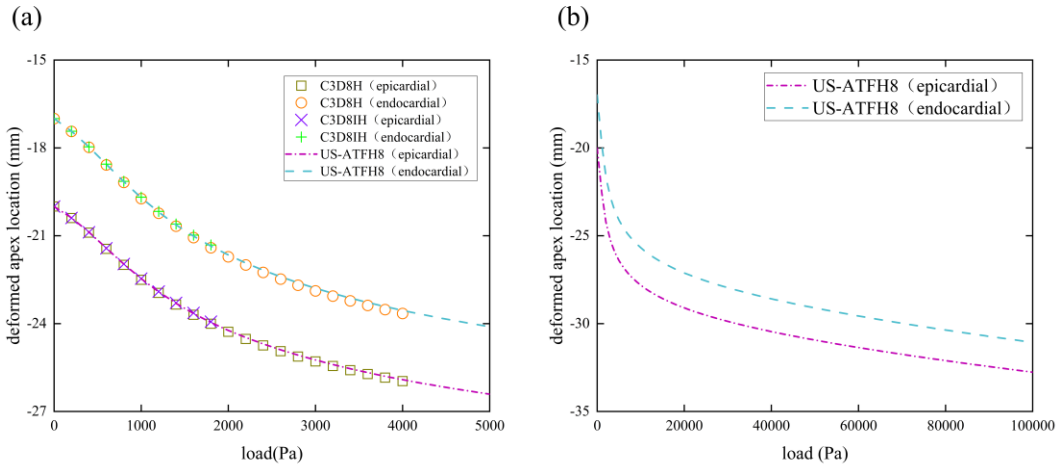

Figure 19. (a) The comparison of deformed location of endocardial and epicardial apex points (under up to 5kPa inner pressure) obtained by US-ATFH8 and other elements. (b) The deformed location of endocardial and epicardial apex points obtained by element US-ATFH8 under up to 100kPa inner pressure.

5. Concluding remarks

This paper extends the unsymmetric 8-node hexahedral element US-ATFH8 [53, 62] based on the ATFs to the analysis of nearly-incompressible hyperelastic soft tissues. This formulation is low-order and only possess conventional displacement DOFs, meaning that the amount of computation can be significantly reduced in large-scale

calculations. The new formulation is insensitive to mesh distortion and avoids volume locking in nearly-incompressible problems. For nonlinear large deformation problems, low-order element with conventional displacement DOFs are usually preferred because of its simplicity and efficiency. This unsymmetric finite element method based on the ATFs provides an effective low-order method for dealing with complicated nearly-incompressible problems in cardiac mechanics and solid mechanics.

One of the key technologies is the use of two different sets of interpolation functions in the test function and trial function, which leads to good precision and mesh distortion tolerance. Another key innovation is that the linear analytical general solutions for anisotropic elasticity is first introduced into the trial functions, which are proved to be good approximations in each increment and greatly improve the element performance. The stresses are computed by an algorithm for updating the deformation gradient interpolated by the anisotropic ATFs described in local skew coordinates [60]. Additionally, the consistent tangent modulus for general anisotropic hyperelastic material is first adopted to update the ATFs in each increment which ensures the rapid convergence for the suggested formulation.

A range of numerical tests are presented to illustrate the performance of the proposed formulation US-ATFH8 in modelling nearly-incompressible anisotropic hyperelastic materials with finite deformation. Especially, element US-ATFH8 can perform well when extreme mesh distortion occurs, while other formulations work poorly or even fail.

The proposed element model provides a universal framework of the unsymmetric finite element method based on the ATFs for finite deformation problems. The update of the ATFs using consistent tangent modulus is suitable for both isotropic and anisotropic materials. The anisotropic hyperelastic formulation described in this paper naturally captures the isotropic hyperelastic and the pure geometric nonlinear cases. For other anisotropic hyperelastic materials, such as polymer foams, hydrogels and meta-materials, as long as the ATFs can be updated properly from the constitutive relation described by the strain energy potential, the present formulations will also exhibit good applicability. Related results will be reported in the near future.

Acknowledgments

The financial support from the National Natural Science Foundation of China (11872229) is greatly appreciated.

Reference

[1] G. Chagnon, M. Rebouah, D. Favier, Hyperelastic Energy Densities for Soft Biological Tissues: A Review, Journal of Elasticity, 120 (2014) 129-160.
[2] R.H. Bhana, A.B. Magan, Lung Mechanics: A Review of Solid Mechanical Elasticity in Lung Parenchyma, Journal of Elasticity, (2023).
[3] J.M. Wakeling, M. Febrer-Nafría, F. De Groote, A review of the efforts to develop muscle and musculoskeletal models for biomechanics in the last 50 years, Journal of Biomechanics, (2023) 111657.
[4] L.A. Mansilla Alvarez, G.D. Ares, R.A. Feijóo, P.J. Blanco, A mixed-order interpolation solid element for efficient arterial wall simulations, Computational Mechanics, (2023).
[5] T.C. Gasser, R.W. Ogden, G.A. Holzapfel, Hyperelastic modelling of arterial layers with distributed collagen fibre orientations, Journal of The Royal Society Interface, 3 (2005) 15-35.
[6] D.R. Nolan, A.L. Gower, M. Destrade, R.W. Ogden, J.P. McGarry, A robust anisotropic hyperelastic formulation for the modelling of soft tissue, Journal of the Mechanical Behavior of Biomedical Materials, 39 (2014) 48-60.
[7] C. Castillo-Méndez, A. Ortiz, Role of anisotropic invariants in numerically modeling soft biological tissues as transversely isotropic hyperelastic materials: A comparative study, International Journal of Non-Linear Mechanics, 138 (2022) 103833.
[8] Y.C. Fung, Biomechanics: mechanical properties of living tissues, Springer Science & Business Media, 2013.
[9] A.N. Smuts, D.C. Blaine, C. Scheffer, H. Weich, A.F. Doubell, K.H. Dellimore, Application of finite element analysis to the design of tissue leaflets for a percutaneous aortic valve, Journal of the Mechanical Behavior of Biomedical Materials, 4 (2011) 85-98.
[10] R. Shaheen, M. Doumit, Modelling a soft composite accumulator for human mobility assist devices, Journal of the Mechanical Behavior of Biomedical Materials, 80 (2018) 81-87.
[11] K. Li, H. Zhao, W. Liu, Z. Yin, Material Properties and Constitutive Modeling of Infant Porcine Cerebellum Tissue in Tension at High Strain Rate, Plos One, 10 (2015).
[12] C. Flynn, A. Taberner, P. Nielsen, Modeling the Mechanical Response of In Vivo Human Skin Under a Rich Set of Deformations, Annals of Biomedical Engineering, 39 (2011) 1935-1946.
[13] Abaqus 2022 Online Documentation, 2022.
[14] S. Land, V. Gurev, S. Arens, C.M. Augustin, L. Baron, R. Blake, C. Bradley, S. Castro, A. Crozier, M. Favino, T.E. Fastl, T. Fritz, H. Gao, A. Gizzi, B.E. Griffith, D.E. Hurtado, R. Krause, X. Luo, M.P. Nash, S. Pezzuto, G. Plank, S. Rossi, D. Ruprecht, G. Seemann, N.P. Smith, J. Sundnes, J.J. Rice, N. Trayanova, D. Wang, Z. Jenny Wang, S.A. Niederer, Verification of cardiac mechanics software: benchmark problems and solutions for testing active and passive material behaviour, Proceedings of the Royal

Society A: Mathematical, Physical and Engineering Sciences, 471 (2015) 20150641.
[15] J.O. Campos, R.W. dos Santos, J. Sundnes, B.M. Rocha, Preconditioned augmented Lagrangian formulation for nearly incompressible cardiac mechanics, International Journal for Numerical Methods in Biomedical Engineering, 34 (2018) e2948.
[16] K.S. Chavan, B.P. Lamichhane, B.I. Wohlmuth, Locking-free finite element methods for linear and nonlinear elasticity in 2D and 3D, Computer Methods in Applied Mechanics and Engineering, 196 (2007) 4075-4086.
[17] A. Propp, A. Gizzi, F. Levrero-Florencio, R. Ruiz-Baier, An orthotropic electro-viscoelastic model for the heart with stress-assisted diffusion, Biomechanics and Modeling in Mechanobiology, 19 (2020) 633-659.
[18] R. Ruiz-Baier, A. Gizzi, A. Loppini, C. Cherubini, S. Filippi, Modelling Thermo-Electro-Mechanical Effects in Orthotropic Cardiac Tissue, Communications in Computational Physics, 1 (2019) 87-115.
[19] P.E. Farrell, L.F. Gatica, B.P. Lamichhane, R. Oyarzúa, R. Ruiz-Baier, Mixed Kirchhoff stress–displacement–pressure formulations for incompressible hyperelasticity, Computer Methods in Applied Mechanics and Engineering, 374 (2021) 113562.
[20] E. Karabelas, G. Haase, G. Plank, C.M. Augustin, Versatile stabilized finite element formulations for nearly and fully incompressible solid mechanics, Computational Mechanics, 65 (2020) 193-215.
[21] G. Scovazzi, B. Carnes, X. Zeng, S. Rossi, A simple, stable, and accurate linear tetrahedral finite element for transient, nearly, and fully incompressible solid dynamics: a dynamic variational multiscale approach, International Journal for Numerical Methods in Engineering, 106 (2016) 799-839.
[22] D. Baroli, A. Quarteroni, R. Ruiz-Baier, Convergence of a stabilized discontinuous Galerkin method for incompressible nonlinear elasticity, Advances in Computational Mathematics, 39 (2013) 425-443.
[23] S. Land, S.A. Niederer, N.P. Smith, Efficient Computational Methods for Strongly Coupled Cardiac Electromechanics, IEEE Transactions on Biomedical Engineering, 59 (2012) 1219-1228.
[24] V. Gurev, P. Pathmanathan, J.-L. Fattebert, H.-F. Wen, J. Magerlein, R.A. Gray, D.F. Richards, J.J. Rice, A high-resolution computational model of the deforming human heart, Biomechanics and modeling in mechanobiology, 14 (2015) 829-849.
[25] S. Land, S.A. Niederer, P. Lamata, N.P. Smith, Improving the Stability of Cardiac Mechanical Simulations, IEEE Transactions on Biomedical Engineering, 62 (2015) 939-947.
[26] C. Bradley, A. Bowery, R. Britten, V. Budelmann, O. Camara, R. Christie, A. Cookson, A.F. Frangi, T.B. Gamage, T. Heidlauf, S. Krittian, D. Ladd, C. Little, K. Mithraratne, M. Nash, D. Nickerson, P. Nielsen, Ø. Nordbø, S. Omholt, A. Pashaei, D. Paterson, V. Rajagopal, A. Reeve, O. Röhrle, S. Safaei, R. Sebastián, M. Steghöfer, T. Wu, T. Yu, H. Zhang, P. Hunter, OpenCMISS: A multi-physics & multi-scale

computational infrastructure for the VPH/Physiome project, Progress in Biophysics and Molecular Biology, 107 (2011) 32-47.
[27] S. Pezzuto, D. Ambrosi, A. Quarteroni, An orthotropic active–strain model for the myocardium mechanics and its numerical approximation, European Journal of Mechanics - A/Solids, 48 (2014) 83-96.
[28] S.-W. Wu, D.-T. Wan, C. Jiang, X. Liu, K. Liu, G.R. Liu, A finite strain model for multi-material, multi-component biomechanical analysis with total Lagrangian smoothed finite element method, International Journal of Mechanical Sciences, 243 (2023) 108017.
[29] H. Gao, H. Wang, C. Berry, X. Luo, B.E. Griffith, Quasi-static image-based immersed boundary-finite element model of left ventricle under diastolic loading, International Journal for Numerical Methods in Biomedical Engineering, 30 (2014) 1199-1222.
[30] T.P. Usyk, A.D. McCulloch, Computational Methods for Soft Tissue Biomechanics, in: G.A. Holzapfel, R.W. Ogden (Eds.) Biomechanics of Soft Tissue in Cardiovascular Systems, Springer Vienna, Vienna, 2003, pp. 273-342.
[31] R.C.P. Kerckhoffs, P.H.M. Bovendeerd, J.C.S. Kotte, F.W. Prinzen, K. Smits, T. Arts, Homogeneity of Cardiac Contraction Despite Physiological Asynchrony of Depolarization: A Model Study, Annals of Biomedical Engineering, 31 (2003) 536-547.
[32] T.P. Usyk, I.J. LeGrice, A.D. McCulloch, Computational model of three-dimensional cardiac electromechanics, Computing and Visualization in Science, 4 (2002) 249-257.
[33] F.J. Vetter, A.D. McCulloch, Three-Dimensional Stress and Strain in Passive Rabbit Left Ventricle: A Model Study, Annals of Biomedical Engineering, 28 (2000) 781-792.
[34] T.P. Usyk, R. Mazhari, A.D. McCulloch, Effect of Laminar Orthotropic Myofiber Architecture on Regional Stress and Strain in the Canine Left Ventricle, Journal of elasticity and the physical science of solids, 61 (2000) 143-164.
[35] M. Hadjicharalambous, J. Lee, N.P. Smith, D.A. Nordsletten, A displacement-based finite element formulation for incompressible and nearly-incompressible cardiac mechanics, Computer Methods in Applied Mechanics and Engineering, 274 (2014) 213-236.
[36] T.J.R. Hughes, Generalization of selective integration procedures to anisotropic and nonlinear media, International Journal for Numerical Methods in Engineering, 15 (1980) 1413-1418.
[37] B. Moran, M. Ortiz, C.F. Shih, Formulation of implicit finite element methods for multiplicative finite deformation plasticity, International Journal for Numerical Methods in Engineering, 29 (1990) 483-514.
[38] E.A. de Souza Neto, D. Perić, M. Dutko, D.R.J. Owen, Design of simple low order finite elements for large strain analysis of nearly incompressible solids, International Journal of Solids and Structures, 33 (1996) 3277-3296.
[39] E.A.d.S. Neto, F.M.A. Pires, D.R.J. Owen, F-bar-based linear triangles and

tetrahedra for finite strain analysis of nearly incompressible solids. Part I: formulation and benchmarking, International Journal for Numerical Methods in Engineering, 62 (2005) 353-383.
[40] A. Masud, T.J. Truster, A framework for residual-based stabilization of incompressible finite elasticity: Stabilized formulations and $\bar{F}$ methods for linear triangles and tetrahedra, Computer Methods in Applied Mechanics and Engineering, 267 (2013) 359-399.
[41] A.K. Sharma, M.M. Joglekar, A computationally efficient locking free numerical framework for modeling visco-hyperelastic dielectric elastomers, Computer Methods in Applied Mechanics and Engineering, 352 (2019) 625-653.
[42] A.K. Sharma, M.M. Joglekar, A numerical framework for modeling anisotropic dielectric elastomers, Computer Methods in Applied Mechanics and Engineering, 344 (2019) 402-420.
[43] A.K. Sharma, A. Khurana, M.M. Joglekar, A Finite Element Model for Investigating the Thermo-Electro-Mechanical Response of Inhomogeneously Deforming Dielectric Elastomer Actuators, European Journal of Computational Mechanics, 30 (2021) 387–408.
[44] S. Doll, K. Schweizerhof, R. Hauptmann, C. Freischläger, On volumetric locking of low‐order solid and solid‐shell elements for finite elastoviscoplastic deformations and selective reduced integration, Engineering Computations, 17 (2000) 874-902.
[45] T. Belytschko, L.P. Bindeman, Assumed strain stabilization of the 4-node quadrilateral with 1-point quadrature for nonlinear problems, Computer Methods in Applied Mechanics and Engineering, 88 (1991) 311-340.
[46] J.C. Simo, F. Armero, Geometrically non-linear enhanced strain mixed methods and the method of incompatible modes, International Journal for Numerical Methods in Engineering, 33 (1992) 1413-1449.
[47] M.A. Crisfield, G.F. Moita, A co-rotational formulation for 2-d continua including incompatible modes, International Journal for Numerical Methods in Engineering, 39 (1996) 2619-2633.
[48] J. Liu, C.C. Foo, Z.-Q. Zhang, A 3D multi-field element for simulating the electromechanical coupling behavior of dielectric elastomers, Acta Mechanica Solida Sinica, 30 (2017) 374-389.
[49] E.T. Ooi, S. Rajendran, J.H. Yeo, A 20-node hexahedron element with enhanced distortion tolerance, International Journal for Numerical Methods in Engineering, 60 (2004) 2501-2530.
[50] S. Rajendran, K.M. Liew, A novel unsymmetric 8-node plane element immune to mesh distortion under a quadratic displacement field, International Journal for Numerical Methods in Engineering, 58 (2003) 1713-1748.
[51] E. Tat Ooi, S. Rajendran, J. Hock Yeo, Extension of unsymmetric finite elements US‐QUAD8 and US‐HEXA20 for geometric nonlinear analyses, Engineering Computations, 24 (2007) 407-431.
[52] S. Cen, P.-L. Zhou, C.-F. Li, C.-J. Wu, An unsymmetric 4-node, 8-DOF plane

membrane element perfectly breaking through MacNeal's theorem, International Journal for Numerical Methods in Engineering, 103 (2015) 469-500.
[53] P.-L. Zhou, S. Cen, J.-B. Huang, C.-F. Li, Q. Zhang, An unsymmetric 8-node hexahedral element with high distortion tolerance, International Journal for Numerical Methods in Engineering, 109 (2016) 1130-1158.
[54] J. Huang, S. Cen, Z. Li, C.-F. Li, An unsymmetric 8-node hexahedral solid-shell element with high distortion tolerance: Linear formulations, International Journal for Numerical Methods in Engineering, 116 (2018) 759-783.
[55] Z. Li, S. Cen, C.-J. Wu, Y. Shang, C.-F. Li, High-performance geometric nonlinear analysis with the unsymmetric 4-node, 8-DOF plane element US-ATFQ4, International Journal for Numerical Methods in Engineering, 114 (2018) 931-954.
[56] Z. Li, J. Huang, S. Cen, C.-F. Li, An unsymmetric 8-node hexahedral solid-shell element with high distortion tolerance: Geometric nonlinear formulations, International Journal for Numerical Methods in Engineering, 120 (2019) 580-606.
[57] Y.-Q. Long, S. Cen, Z.-F. Long, Advanced finite element method in structural engineering, Springer, 2009.
[58] S. Cen, X.-M. Chen, C.F. Li, X.-R. Fu, Quadrilateral membrane elements with analytical element stiffness matrices formulated by the new quadrilateral area coordinate method (QACM-II), International Journal for Numerical Methods in Engineering, 77 (2009) 1172-1200.
[59] X.-M. Chen, S. Cen, X.-R. Fu, Y.-Q. Long, A new quadrilateral area coordinate method (QACM-II) for developing quadrilateral finite element models, International Journal for Numerical Methods in Engineering, 73 (2008) 1911-1941.
[60] K.Y. Yuan, Y.S. Huang, H.T. Yang, T.H.H. Pian, The inverse mapping and distortion measures for 8-node hexahedral isoparametric elements, Computational Mechanics, 14 (1994) 189-199.
[61] Z. Li, S. Cen, J. Huang, C.F. Li, Hyperelastic finite deformation analysis with the unsymmetric finite element method containing homogeneous solutions of linear elasticity, International Journal for Numerical Methods in Engineering, (2020).
[62] R.-X. Ma, S. Cen, Y. Shang, C.-F. Li, Extension of the unsymmetric 8-node hexahedral solid element US-ATFH8 to 3D hyper-elastic finite deformation analysis, International Journal for Numerical Methods in Engineering, n/a (2022).
[63] Y. Huang, Y. Huan, H. Chen, An incompatible and unsymmetric four-node quadrilateral plane element with high numerical performance, International Journal for Numerical Methods in Engineering, 121 (2020) 3382-3396.
[64] Y.-Q. Huang, Y.-F. Yang, J.-Z. Wang, X.-C. Liu, H.-B. Chen, Unsymmetric extensions of Wilson's incompatible four-node quadrilateral and eight-node hexahedral elements, International Journal for Numerical Methods in Engineering, n/a (2021).
[65] R. Pfefferkorn, P. Betsch, Mesh Distortion Insensitive and Locking-free Petrov-Galerkin low-order EAS Elements for Linear Elasticity, International Journal for Numerical Methods in Engineering, n/a (2021).
[66] R. Pfefferkorn, P. Betsch, Hourglassing- and Locking-Free Mesh Distortion

Insensitive Petrov-Galerkin EAS Element for Large Deformation Solid Mechanics, International Journal for Numerical Methods in Engineering, n/a (2022).
[67] T. Cowan, W.M. Coombs, Rotationally invariant distortion resistant finite-elements, Computer Methods in Applied Mechanics and Engineering, 275 (2014) 189-203.
[68] A. Bijalwan, B.P. Patel, M. Marieswaran, D. Kalyanasundaram, Volumetric locking free 3D finite element for modelling of anisotropic visco-hyperelastic behaviour of anterior cruciate ligament, Journal of Biomechanics, 73 (2018) 1-8.
[69] I.I. Tagiltsev, A.V. Shutov, Geometrically nonlinear modelling of pre-stressed viscoelastic fibre-reinforced composites with application to arteries, Biomechanics and Modeling in Mechanobiology, 20 (2021) 323-337.
[70] J.M. Vassoler, L. Stainier, E.A. Fancello, A variational framework for fiber-reinforced viscoelastic soft tissues including damage, International Journal for Numerical Methods in Engineering, 108 (2016) 865-884.
[71] E. Pena, B. Calvo, M.A. Martinez, M. Doblare, On finite-strain damage of viscoelastic-fibred materials. Application to soft biological tissues, International Journal for Numerical Methods in Engineering, 74 (2008) 1198-1218.
[72] G.A. Holzapfel, Nonlinear solid mechanics: a continuum approach for engineering science, in, Kluwer Academic Publishers Dordrecht, 2002.
[73] J.C. Simo, R.L. Taylor, Penalty function formulations for incompressible nonlinear elastostatics, Computer Methods in Applied Mechanics and Engineering, 35 (1982) 107-118.
[74] K.C.L. Wong, L. Wang, P. Shi, Active Model with Orthotropic Hyperelastic Material for Cardiac Image Analysis, in: N. Ayache, H. Delingette, M. Sermesant (Eds.) Functional Imaging and Modeling of the Heart, Springer Berlin Heidelberg, Berlin, Heidelberg, 2009, pp. 229-238.
[75] W. Sun, E.L. Chaikof, M.E. Levenston, Numerical Approximation of Tangent Moduli for Finite Element Implementations of Nonlinear Hyperelastic Material Models, Journal of Biomechanical Engineering, 130 (2008).
[76] C. Miehe, Numerical computation of algorithmic (consistent) tangent moduli in large-strain computational inelasticity, Computer Methods in Applied Mechanics and Engineering, 134 (1996) 223-240.
[77] J. Korelc, P. Wriggers, Automation of Finite Element Methods, 2016.
[78] J.D. Bayer, R.C. Blake, G. Plank, N.A. Trayanova, A novel rule-based algorithm for assigning myocardial fiber orientation to computational heart models, Annals of biomedical engineering, 40 (2012) 2243-2254.

Appendix A. The three-dimensional skew coordinate system

For a 3D hexahedron 8-node element shown in **Figure 2**, the relationship between Cartesian coordinates and isoparametric coordinates is as follows：

$$\begin{Bmatrix} x \\ y \\ z \end{Bmatrix} = \sum_{I=1}^{8} \bar{N}_I \begin{Bmatrix} x_I \\ y_I \\ z_I \end{Bmatrix} = \begin{Bmatrix} x_0 + \bar{a}_1\xi + \bar{a}_2\eta + \bar{a}_3\zeta + \bar{a}_4\xi\eta + \bar{a}_5\eta\zeta + \bar{a}_6\xi\zeta + \bar{a}_7\xi\eta\zeta \\ y_0 + \bar{b}_1\xi + \bar{b}_2\eta + \bar{b}_3\zeta + \bar{b}_4\xi\eta + \bar{b}_5\eta\zeta + \bar{b}_6\xi\zeta + \bar{b}_7\xi\eta\zeta \\ z_0 + \bar{c}_1\xi + \bar{c}_2\eta + \bar{c}_3\zeta + \bar{c}_4\xi\eta + \bar{c}_5\eta\zeta + \bar{c}_6\xi\zeta + \bar{c}_7\xi\eta\zeta \end{Bmatrix} \quad \text{(A.1)}$$

where,

$$\bar{N}_I = \frac{1}{8}(1+\xi_I\xi)(1+\eta_I\eta)(1+\zeta_I\zeta), \qquad i = 1,2,...,8 \quad \text{(A.2)}$$

is the interpolation function of trilinear isoparametric element, and

$$\begin{Bmatrix} x_0 \\ y_0 \\ z_0 \end{Bmatrix} = \frac{1}{8}\sum_{I=1}^{8} \begin{Bmatrix} x_I \\ y_I \\ z_I \end{Bmatrix}, \begin{Bmatrix} \bar{a}_1 \\ \bar{b}_1 \\ \bar{c}_1 \end{Bmatrix} = \frac{1}{8}\sum_{i=1}^{8} \xi_I \begin{Bmatrix} x_I \\ y_I \\ z_I \end{Bmatrix}$$
$$\begin{Bmatrix} \bar{a}_2 \\ \bar{b}_2 \\ \bar{c}_2 \end{Bmatrix} = \frac{1}{8}\sum_{I=1}^{8} \eta_I \begin{Bmatrix} x_I \\ y_I \\ z_I \end{Bmatrix}, \begin{Bmatrix} \bar{a}_3 \\ \bar{b}_3 \\ \bar{c}_3 \end{Bmatrix} = \frac{1}{8}\sum_{I=1}^{8} \zeta_I \begin{Bmatrix} x_I \\ y_I \\ z_I \end{Bmatrix} \quad \text{(A.3)}$$

x_I， y_I， z_I， ξ_I， η_I， ζ_I are the Cartesian coordinates and isoparametric coordinates respectively.

The linear relation between 3D skew coordinates and Cartesian coordinates is determined by the Jacobian matrix $[\mathbf{J}_0]$ defined at the origin of isoparametric coordinate：

$$\begin{Bmatrix} R \\ S \\ T \end{Bmatrix} = ([\mathbf{J}_0]^{-1})^{\mathrm{T}} \left(\begin{Bmatrix} x \\ y \\ z \end{Bmatrix} - \begin{Bmatrix} x \\ y \\ z \end{Bmatrix}_{\xi=\eta=\zeta=0} \right) = \frac{1}{J_0} \begin{bmatrix} a_1 & b_1 & c_1 \\ a_2 & b_2 & c_2 \\ a_3 & b_3 & c_3 \end{bmatrix} \begin{Bmatrix} x - x_0 \\ y - y_0 \\ z - z_0 \end{Bmatrix} \quad \text{(A.4)}$$

$$[\mathbf{J}_0]=\left[\begin{array}{ccc}\dfrac{\partial x}{\partial \xi} & \dfrac{\partial y}{\partial \xi} & \dfrac{\partial z}{\partial \xi}\\ \dfrac{\partial x}{\partial \eta} & \dfrac{\partial y}{\partial \eta} & \dfrac{\partial z}{\partial \eta}\\ \dfrac{\partial x}{\partial \zeta} & \dfrac{\partial y}{\partial \zeta} & \dfrac{\partial z}{\partial \zeta}\end{array}\right]_{\xi=\eta=\zeta=0}=\left[\begin{array}{ccc}\bar{a}_1 & \bar{b}_1 & \bar{c}_1\\ \bar{a}_2 & \bar{b}_2 & \bar{c}_2\\ \bar{a}_3 & \bar{b}_3 & \bar{c}_3\end{array}\right] \tag{A.5}$$

$$\begin{aligned}
&J_0=\left|[\mathbf{J}_0]\right|=\bar{a}_1(\bar{b}_2\bar{c}_3-\bar{b}_3\bar{c}_2)+\bar{a}_2(\bar{b}_3\bar{c}_1-\bar{b}_1\bar{c}_3)+\bar{a}_3(\bar{b}_1\bar{c}_2-\bar{b}_2\bar{c}_1)\\
&\quad=\bar{a}_1a_1+\bar{a}_2a_2+\bar{a}_3a_3=\bar{b}_1b_1+\bar{b}_2b_2+\bar{b}_3b_3=\bar{c}_1c_1+\bar{c}_2c_2+\bar{c}_3c_3\\
&a_1=\bar{b}_2\bar{c}_3-\bar{b}_3\bar{c}_2,\qquad b_1=\bar{a}_3\bar{c}_2-\bar{a}_2\bar{c}_3,\qquad c_1=\bar{a}_2\bar{b}_3-\bar{a}_3\bar{b}_2\\
&a_2=\bar{b}_3\bar{c}_1-\bar{b}_1\bar{c}_3,\qquad b_2=\bar{a}_1\bar{c}_3-\bar{a}_3\bar{c}_1,\qquad c_2=\bar{a}_3\bar{b}_1-\bar{a}_1\bar{b}_3\\
&a_3=\bar{b}_1\bar{c}_2-\bar{b}_2\bar{c}_1,\qquad b_3=\bar{a}_2\bar{c}_1-\bar{a}_1\bar{c}_2,\qquad c_3=\bar{a}_1\bar{b}_2-\bar{a}_2\bar{b}_1
\end{aligned} \tag{A.6}$$

In addition, to facilitate the derivation of three-dimensional analytical solutions, the following parameters are defined：

$$\begin{aligned}
&h_1=\bar{b}_2\bar{c}_3+\bar{b}_3\bar{c}_2,\qquad h_2=\bar{a}_2\bar{c}_3+\bar{a}_3\bar{c}_2,\qquad h_3=\bar{a}_2\bar{b}_3+\bar{a}_3\bar{b}_2\\
&h_4=\bar{b}_1\bar{c}_3+\bar{b}_3\bar{c}_1,\qquad h_5=\bar{a}_1\bar{c}_3+\bar{a}_3\bar{c}_1,\qquad h_6=\bar{a}_1\bar{b}_3+\bar{a}_3\bar{b}_1\\
&h_7=\bar{b}_1\bar{c}_2+\bar{b}_2\bar{c}_1,\qquad h_8=\bar{a}_1\bar{c}_2+\bar{a}_2\bar{c}_1,\qquad h_9=\bar{a}_1\bar{b}_2+\bar{a}_2\bar{b}_1
\end{aligned} \tag{A.7}$$

Appendix B. Anisotropic analytical homogeneous solutions for quadratic displacements in skew coordinates

（1）The 13th–15th sets (j = 13–15) of analytical general solutions for quadratic displacements

$$\begin{aligned}
U_i=&\frac{1}{2J_0}\{[\bar{a}_1J_0A_{xi}+(J_0-\bar{a}_1a_1)(\bar{a}_1A_{xi}+\bar{b}_1A_{xyi}+\bar{c}_1A_{zxi})-a_1(\bar{b}_1^2A_{yi}+\bar{c}_1^2A_{zi}+\bar{b}_1\bar{c}_1A_{yzi})]R^2\\
&-a_1(\bar{a}_2^2A_{xi}+\bar{b}_2^2A_{yi}+\bar{c}_2^2A_{zi}+\bar{a}_2\bar{b}_2A_{xyi}+\bar{b}_2\bar{c}_2A_{yzi}+\bar{a}_2\bar{c}_2A_{zxi})S^2-a_1(\bar{a}_3^2A_{xi}+\bar{b}_3^2A_{yi}\\
&+\bar{c}_3^2A_{zi}+\bar{a}_3\bar{b}_3A_{xyi}+\bar{b}_3\bar{c}_3A_{yzi}+\bar{a}_3\bar{c}_3A_{zxi})T^2+[J_0(2\bar{a}_2A_{xi}+\bar{b}_2A_{xyi}+\bar{c}_2A_{zxi})-2a_1(\bar{a}_1\bar{a}_2A_{xi}\\
&+\bar{b}_1\bar{b}_2A_{yi}+\bar{c}_1\bar{c}_2A_{zi})-a_1(h_9A_{xyi}+h_7A_{yzi}+h_8A_{zxi})]RS+[J_0(2\bar{a}_3A_{xi}+\bar{b}_3A_{xyi}+\bar{c}_3A_{zxi})\\
&-2a_1(\bar{a}_1\bar{a}_3A_{xi}+\bar{b}_1\bar{b}_3A_{yi}+\bar{c}_1\bar{c}_3A_{zi})-a_1(h_6A_{xyi}+h_4A_{yzi}+h_5A_{zxi})]RT-a_1(2\bar{a}_2\bar{a}_3A_{xi}+2\bar{b}_2\bar{b}_3A_{yi}\\
&+2\bar{c}_2\bar{c}_3A_{zi}+h_3A_{xyi}+h_1A_{yzi}+h_2A_{zxi})ST\}
\end{aligned} \tag{B.1}$$

$$V_i=\frac{1}{2J_0}\{[\bar{b}_1J_0A_{yi}+(J_0-\bar{b}_1b_1)(\bar{a}_1A_{xyi}+\bar{b}_1A_{yi}+\bar{c}_1A_{yzi})-b_1(\bar{a}_1^2A_{xi}+\bar{c}_1^2A_{zi}+\bar{a}_1\bar{c}_1A_{zxi})]R^2$$
$$-b_1(\bar{a}_2^2A_{xi}+\bar{b}_2^2A_{yi}+\bar{c}_2^2A_{zi}+\bar{a}_2\bar{b}_2A_{xyi}+\bar{b}_2\bar{c}_2A_{yzi}+\bar{a}_2\bar{c}_2A_{zxi})S^2-b_1(\bar{a}_3^2A_{xi}+\bar{b}_3^2A_{yi}$$
$$+\bar{c}_3^2A_{zi}+\bar{a}_3\bar{b}_3A_{xyi}+\bar{b}_3\bar{c}_3A_{yzi}+\bar{a}_3\bar{c}_3A_{zxi})T^2+[J_0(\bar{a}_2A_{xyi}+2\bar{b}_2A_{yi}+\bar{c}_2A_{yzi})-2b_1(\bar{a}_1\bar{a}_2A_{xi}$$
$$+\bar{b}_1\bar{b}_2A_{yi}+\bar{c}_1\bar{c}_2A_{zi})-b_1(h_9A_{xyi}+h_7A_{yzi}+h_8A_{zxi})]RS+[J_0(\bar{a}_3A_{xyi}+2\bar{b}_3A_{yi}+\bar{c}_3A_{yzi})$$
$$-2b_1(\bar{a}_1\bar{a}_3A_{xi}+\bar{b}_1\bar{b}_3A_{yi}+\bar{c}_1\bar{c}_3A_{zi})-b_1(h_6A_{xyi}+h_4A_{yzi}+h_5A_{zxi})]RT-b_1(2\bar{a}_2\bar{a}_3A_{xi}+2\bar{b}_2\bar{b}_3A_{yi}$$
$$+2\bar{c}_2\bar{c}_3A_{zi}+h_3A_{xyi}+h_1A_{yzi}+h_2A_{zxi})ST\}$$

(B.2)

$$W_i=\frac{1}{2J_0}\{[\bar{c}_1J_0A_{zi}+(J_0-\bar{c}_1c_1)(\bar{a}_1A_{zxi}+\bar{b}_1A_{yzi}+\bar{c}_1A_{zi})-\bar{c}_1(\bar{a}_1^2A_{xi}+\bar{b}_1^2A_{yi}+\bar{a}_1\bar{b}_1A_{xyi})]R^2$$
$$-c_1(\bar{a}_2^2A_{xi}+\bar{b}_2^2A_{yi}+\bar{c}_2^2A_{zi}+\bar{a}_2\bar{b}_2A_{xyi}+\bar{b}_2\bar{c}_2A_{yzi}+\bar{a}_2\bar{c}_2A_{zxi})S^2-c_1(\bar{a}_3^2A_{xi}+\bar{b}_3^2A_{yi}$$
$$+\bar{c}_3^2A_{zi}+\bar{a}_3\bar{b}_3A_{xyi}+\bar{b}_3\bar{c}_3A_{yzi}+\bar{a}_3\bar{c}_3A_{zxi})T^2+[J_0(\bar{a}_2A_{zxi}+\bar{b}_2A_{yzi}+2\bar{c}_2A_{zi})-2c_1(\bar{a}_1\bar{a}_2A_{xi}$$
$$+\bar{b}_1\bar{b}_2A_{yi}+\bar{c}_1\bar{c}_2A_{zi})-c_1(h_9A_{xyi}+h_7A_{yzi}+h_8A_{zxi})]RS+[J_0(\bar{a}_3A_{zxi}+\bar{b}_3A_{yzi}+2\bar{c}_3A_{zi})$$
$$-2c_1(\bar{a}_1\bar{a}_3A_{xi}+\bar{b}_1\bar{b}_3A_{yi}+\bar{c}_1\bar{c}_3A_{zi})-c_1(h_6A_{xyi}+h_4A_{yzi}+h_5A_{zxi})]RT-c_1(2\bar{a}_2\bar{a}_3A_{xi}+2\bar{b}_2\bar{b}_3A_{yi}$$
$$+2\bar{c}_2\bar{c}_3A_{zi}+h_3A_{xyi}+h_1A_{yzi}+h_2A_{zxi})ST\}$$

(B.3)

（2）The 16th–18th sets (j = 16–18) of analytical general solutions for quadratic displacements

$$U_i=\frac{1}{2J_0}\{-a_2(\bar{a}_1^2A_{xi}+\bar{b}_1^2A_{yi}+\bar{c}_1^2A_{zi}+\bar{a}_1\bar{b}_1A_{xyi}+\bar{b}_1\bar{c}_1A_{yzi}+\bar{a}_1\bar{c}_1A_{zxi})R^2+[\bar{a}_2J_0A_{xi}+(J_0$$
$$-\bar{a}_2a_2)(\bar{a}_2A_{xi}+\bar{b}_2A_{xyi}+\bar{c}_2A_{zxi})-a_2(\bar{b}_2^2A_{yi}+\bar{c}_2^2A_{zi}+\bar{b}_2\bar{c}_2A_{yzi})]S^2-a_2(\bar{a}_3^2A_{xi}+\bar{b}_3^2A_{yi}$$
$$+\bar{c}_3^2A_{zi}+\bar{a}_3\bar{b}_3A_{xyi}+\bar{b}_3\bar{c}_3A_{yzi}+\bar{a}_3\bar{c}_3A_{zxi})T^2+[J_0(2\bar{a}_1A_{xi}+\bar{b}_1A_{xyi}+\bar{c}_1A_{zxi})-2a_2(\bar{a}_1\bar{a}_2A_{xi}$$
$$+\bar{b}_1\bar{b}_2A_{yi}+\bar{c}_1\bar{c}_2A_{zi})-a_2(h_9A_{xyi}+h_7A_{yzi}+h_8A_{zxi})]RS-a_2(2\bar{a}_1\bar{a}_3A_{xi}+2\bar{b}_1\bar{b}_3A_{yi}+2\bar{c}_1\bar{c}_3A_{zi}$$
$$+h_6A_{xyi}+h_4A_{yzi}+h_5A_{zxi})RT+[J_0(2\bar{a}_3A_{xi}+\bar{b}_3A_{xyi}+\bar{c}_3A_{zxi})-2a_2(\bar{a}_2\bar{a}_3A_{xi}+\bar{b}_2\bar{b}_3A_{yi}$$
$$+\bar{c}_2\bar{c}_3A_{zi})-a_2(h_3A_{xyi}+h_1A_{yzi}+h_2A_{zxi})]ST\}$$

(B.4)

$$V_i=\frac{1}{2J_0}\{-b_2(\bar{a}_1^2A_{xi}+\bar{b}_1^2A_{yi}+\bar{c}_1^2A_{zi}+\bar{a}_1\bar{b}_1A_{xyi}+\bar{b}_1\bar{c}_1A_{yzi}+\bar{a}_1\bar{c}_1A_{zxi})R^2+[\bar{b}_2J_0A_{yi}+(J_0$$
$$-\bar{b}_2b_2)(\bar{a}_2A_{xyi}+\bar{b}_2A_{yi}+\bar{c}_2A_{yzi})-b_2(\bar{a}_2^2A_{xi}+\bar{c}_2^2A_{zi}+\bar{a}_2\bar{c}_2A_{zxi})]S^2-b_2(\bar{a}_3^2A_{xi}+\bar{b}_3^2A_{yi}$$
$$+\bar{c}_3^2A_{zi}+\bar{a}_3\bar{b}_3A_{xyi}+\bar{b}_3\bar{c}_3A_{yzi}+\bar{a}_3\bar{c}_3A_{zxi})T^2+[J_0(\bar{a}_1A_{xyi}+2\bar{b}_1A_{yi}+\bar{c}_1A_{yzi})-2b_2(\bar{a}_1\bar{a}_2A_{xi}$$
$$+\bar{b}_1\bar{b}_2A_{yi}+\bar{c}_1\bar{c}_2A_{zi})-b_2(h_9A_{xyi}+h_7A_{yzi}+h_8A_{zxi})]RS-b_2(2\bar{a}_1\bar{a}_3A_{xi}+2\bar{b}_1\bar{b}_3A_{yi}+2\bar{c}_1\bar{c}_3A_{zi}$$
$$+h_6A_{xyi}+h_4A_{yzi}+h_5A_{zxi})RT+[J_0(\bar{a}_3A_{xyi}+2\bar{b}_3A_{yi}+\bar{c}_3A_{yzi})-2b_2(\bar{a}_2\bar{a}_3A_{xi}+\bar{b}_2\bar{b}_3A_{yi}$$
$$+\bar{c}_2\bar{c}_3A_{zi})-b_2(h_3A_{xyi}+h_1A_{yzi}+h_2A_{zxi})]ST\}$$

(B.5)

$$W_i = \frac{1}{2J_0}\{-c_2(\bar{a}_1^2 A_{xi} + \bar{b}_1^2 A_{yi} + \bar{c}_1^2 A_{zi} + \bar{a}_1\bar{b}_1 A_{xyi} + \bar{b}_1\bar{c}_1 A_{yzi} + \bar{a}_1\bar{c}_1 A_{zxi})R^2 + [\bar{c}_2 J_0 A_{zi} + (J_0 - \bar{c}_2 c_2)(\bar{a}_2 A_{zxi} + \bar{b}_2 A_{yzi} + \bar{c}_2 A_{zi}) - c_2(\bar{a}_2^2 A_{xi} + \bar{b}_2^2 A_{yi} + \bar{a}_2\bar{b}_2 A_{xyi})]S^2 - c_2(\bar{a}_3^2 A_{xi} + \bar{b}_3^2 A_{yi} + \bar{c}_3^2 A_{zi} + \bar{a}_3\bar{b}_3 A_{xyi} + \bar{b}_3\bar{c}_3 A_{yzi} + \bar{a}_3\bar{c}_3 A_{zxi})T^2 + [J_0(\bar{a}_1 A_{zxi} + \bar{b}_1 A_{yzi} + 2\bar{c}_1 A_{zi}) - 2c_2(\bar{a}_1\bar{a}_2 A_{xi} + \bar{b}_1\bar{b}_2 A_{yi} + \bar{c}_1\bar{c}_2 A_{zi}) - c_2(h_9 A_{xyi} + h_7 A_{yzi} + h_8 A_{zxi})]RS - c_2(2\bar{a}_1\bar{a}_3 A_{xi} + 2\bar{b}_1\bar{b}_3 A_{yi} + 2\bar{c}_1\bar{c}_3 A_{zi} + h_6 A_{xyi} + h_4 A_{yzi} + h_5 A_{zxi})RT + [J_0(\bar{a}_3 A_{zxi} + \bar{b}_3 A_{yzi} + 2\bar{c}_3 A_{zi}) - 2c_2(\bar{a}_2\bar{a}_3 A_{xi} + \bar{b}_2\bar{b}_3 A_{yi} + \bar{c}_2\bar{c}_3 A_{zi}) - c_2(h_3 A_{xyi} + h_1 A_{yzi} + h_2 A_{zxi})]ST\}$$

(B.6)

（3）The 19th–21st sets (j = 19–21) of analytical general solutions for quadratic displacements

$$U_i = \frac{1}{2J_0}\{-a_3(\bar{a}_1^2 A_{xi} + \bar{b}_1^2 A_{yi} + \bar{c}_1^2 A_{zi} + \bar{a}_1\bar{b}_1 A_{xyi} + \bar{b}_1\bar{c}_1 A_{yzi} + \bar{a}_1\bar{c}_1 A_{zxi})R^2 - a_3(\bar{a}_2^2 A_{xi} + \bar{b}_2^2 A_{yi} + \bar{c}_2^2 A_{zi} + \bar{a}_2\bar{b}_2 A_{xyi} + \bar{b}_2\bar{c}_2 A_{yzi} + \bar{a}_2\bar{c}_2 A_{zxi})S^2 + [\bar{a}_3 J_0 A_{xi} + (J_0 - \bar{a}_3 a_3)(\bar{a}_3 A_{xi} + \bar{b}_3 A_{xyi} + \bar{c}_3 A_{zxi}) - a_3(\bar{b}_3^2 A_{yi} + \bar{c}_3^2 A_{zi} + \bar{b}_3\bar{c}_3 A_{yzi})]T^2 - a_3(2\bar{a}_1\bar{a}_2 A_{xi} + 2\bar{b}_1\bar{b}_2 A_{yi} + 2\bar{c}_1\bar{c}_2 A_{zi} + h_9 A_{xyi} + h_7 A_{yzi} + h_8 A_{zxi})RS + [J_0(2\bar{a}_1 A_{xi} + \bar{b}_1 A_{xyi} + \bar{c}_1 A_{zxi}) - 2a_3(\bar{a}_1\bar{a}_3 A_{xi} + \bar{b}_1\bar{b}_3 A_{yi} + \bar{c}_1\bar{c}_3 A_{zi}) - a_3(h_6 A_{xyi} + h_4 A_{yzi} + h_5 A_{zxi})]RT + [J_0(2\bar{a}_2 A_{xi} + \bar{b}_2 A_{xyi} + \bar{c}_2 A_{zxi}) - 2a_3(\bar{a}_2\bar{a}_3 A_{xi} + \bar{b}_2\bar{b}_3 A_{yi} + \bar{c}_2\bar{c}_3 A_{zi}) - a_3(h_3 A_{xyi} + h_1 A_{yzi} + h_2 A_{zxi})]ST\}$$

(B.7)

$$V_i = \frac{1}{2J_0}\{-b_3(\bar{a}_1^2 A_{xi} + \bar{b}_1^2 A_{yi} + \bar{c}_1^2 A_{zi} + \bar{a}_1\bar{b}_1 A_{xyi} + \bar{b}_1\bar{c}_1 A_{yzi} + \bar{a}_1\bar{c}_1 A_{zxi})R^2 - b_3(\bar{a}_2^2 A_{xi} + \bar{b}_2^2 A_{yi} + \bar{c}_2^2 A_{zi} + \bar{a}_2\bar{b}_2 A_{xyi} + \bar{b}_2\bar{c}_2 A_{yzi} + \bar{a}_2\bar{c}_2 A_{zxi})S^2 + [\bar{b}_3 J_0 A_{yi} + (J_0 - \bar{b}_3 b_3)(\bar{a}_3 A_{xyi} + \bar{b}_3 A_{yi} + \bar{c}_3 A_{yzi}) - b_3(\bar{a}_3^2 A_{xi} + \bar{c}_3^2 A_{zi} + \bar{a}_3\bar{c}_3 A_{zxi})]T^2 - b_3(2\bar{a}_1\bar{a}_2 A_{xi} + 2\bar{b}_1\bar{b}_2 A_{yi} + 2\bar{c}_1\bar{c}_2 A_{zi} + h_9 A_{xyi} + h_7 A_{yzi} + h_8 A_{zxi})RS + [J_0(\bar{a}_1 A_{xyi} + 2\bar{b}_1 A_{yi} + \bar{c}_1 A_{yzi}) - 2b_3(\bar{a}_1\bar{a}_3 A_{xi} + \bar{b}_1\bar{b}_3 A_{yi} + \bar{c}_1\bar{c}_3 A_{zi}) - b_3(h_6 A_{xyi} + h_4 A_{yzi} + h_5 A_{zxi})]RT + [J_0(\bar{a}_2 A_{xyi} + 2\bar{b}_2 A_{yi} + \bar{c}_2 A_{yzi}) - 2b_3(\bar{a}_2\bar{a}_3 A_{xi} + \bar{b}_2\bar{b}_3 A_{yi} + \bar{c}_2\bar{c}_3 A_{zi}) - b_3(h_3 A_{xyi} + h_1 A_{yzi} + h_2 A_{zxi})]ST\}$$

(B.8)

$$W_i = \frac{1}{2J_0}\{-c_3(\bar{a}_1^2 A_{xi} + \bar{b}_1^2 A_{yi} + \bar{c}_1^2 A_{zi} + \bar{a}_1\bar{b}_1 A_{xyi} + \bar{b}_1\bar{c}_1 A_{yzi} + \bar{a}_1\bar{c}_1 A_{zxi})R^2 - c_3(\bar{a}_2^2 A_{xi} + \bar{b}_2^2 A_{yi} + \bar{c}_2^2 A_{zi} + \bar{a}_2\bar{b}_2 A_{xyi} + \bar{b}_2\bar{c}_2 A_{yzi} + \bar{a}_2\bar{c}_2 A_{zxi})S^2 + [\bar{c}_3 J_0 A_{zi} + (J_0 - \bar{c}_3 c_3)(\bar{a}_3 A_{zxi} + \bar{b}_3 A_{yzi} + \bar{c}_3 A_{zi}) - c_3(\bar{a}_3^2 A_{xi} + \bar{b}_3^2 A_{yi} + \bar{a}_3\bar{b}_3 A_{xyi})]T^2 - c_3(2\bar{a}_1\bar{a}_2 A_{xi} + 2\bar{b}_1\bar{b}_2 A_{yi} + 2\bar{c}_1\bar{c}_2 A_{zi} + h_9 A_{xyi} + h_7 A_{yzi} + h_8 A_{zxi})RS + [J_0(\bar{a}_1 A_{zxi} + \bar{b}_1 A_{yzi} + 2\bar{c}_1 A_{zi}) - 2c_3(\bar{a}_1\bar{a}_3 A_{xi} + \bar{b}_1\bar{b}_3 A_{yi} + \bar{c}_1\bar{c}_3 A_{zi}) - c_3(h_6 A_{xyi} + h_4 A_{yzi} + h_5 A_{zxi})]RT + [J_0(\bar{a}_2 A_{zxi} + \bar{b}_2 A_{yzi} + 2\bar{c}_2 A_{zi}) - 2c_3(\bar{a}_2\bar{a}_3 A_{xi} + \bar{b}_2\bar{b}_3 A_{yi} + \bar{c}_2\bar{c}_3 A_{zi}) - c_3(h_3 A_{xyi} + h_1 A_{yzi} + h_2 A_{zxi})]ST\} \tag{B.9}$$

Appendix C. Material parameters

The selection of the penalty factor

b_{1111}=1, b_{1122}=0, b_{2222}=1, b_{1133}=0, b_{2233}=0, b_{3333}=1, b_{1112}=0, b_{2212}=0, b_{3312}=0, b_{1212}=0.5, b_{1113}=0, b_{2213}=0, b_{3313}=0, b_{1213}=0, b_{1313}=0.5, b_{1123}=0, b_{2223}=0, b_{3323}=0, b_{1223}=0, b_{1323}=0, b_{2323}=0.5,c =10000

Uniaxial tension and Simple shear

b_{1111}=8, b_{1122}=0, b_{2222}=2, b_{1133}=0, b_{2233}=0, b_{3333}=2, b_{1112}=0, b_{2212}=0, b_{3312}=0, b_{1212}=2, b_{1113}=0, b_{2213}=0, b_{3313}=0, b_{1213}=0, b_{1313}=2, b_{1123}=0, b_{2223}=0, b_{3323}=0, b_{1223}=0, b_{1323}=0, b_{2323}=1,c =2000

Orthotropic hyperelastic soft Cook's beam

b_{1111}=1, b_{1122}=0.5, b_{2222}=1, b_{1133}=0.5, b_{2233}=0.5, b_{3333}=1, b_{1112}=0, b_{2212}=0, b_{3312}=0, b_{1212}=0.5, b_{1113}=0, b_{2213}=0, b_{3313}=0, b_{1213}=0, b_{1313}=0.5, b_{1123}=0, b_{2223}=0, b_{3323}=0, b_{1223}=0, b_{1323}=0, b_{2323}=0.5,c =10000

Orthotropic hyperelastic soft cantilever beam

b_{1111}=0.9925, b_{1122}=0.0749, b_{2222}=0.418, b_{1133}=0.0295, b_{2233}=0.0193, b_{3333}=0.0089, b_{1112}=0, b_{2212}=0, b_{3312}=0, b_{1212}=5, b_{1113}=0, b_{2213}=0, b_{3313}=0, b_{1213}=0, b_{1313}=5, b_{1123}=0,

b_{2223}=0, b_{3323}=0, b_{1223}=0, b_{1323}=0, b_{2323}=5,c =26950

Transversely isotropic soft curved beam

b_{1111}=8**,** b_{1122}=0, b_{2222}=2, b_{1133}=0, b_{2233}=0, b_{3333}=2, b_{1112}=0, b_{2212}=0, b_{3312}=0, b_{1212}=2, b_{1113}=0, b_{2213}=0, b_{3313}=0, b_{1213}=0, b_{1313}=2, b_{1123}=0, b_{2223}=0, b_{3323}=0, b_{1223}=0, b_{1323}=0, b_{2323}=1,c =2000

Transversely isotropic soft beam with a square cross-section

b_{1111}=8**,** b_{1122}=0, b_{2222}=2, b_{1133}=0, b_{2233}=0, b_{3333}=2, b_{1112}=0, b_{2212}=0, b_{3312}=0, b_{1212}=2, b_{1113}=0, b_{2213}=0, b_{3313}=0, b_{1213}=0, b_{1313}=2, b_{1123}=0, b_{2223}=0, b_{3323}=0, b_{1223}=0, b_{1323}=0, b_{2323}=1,c =2000

Benchmark test for transversely isotropic beam

b_{1111}=8**,** b_{1122}=0, b_{2222}=2, b_{1133}=0, b_{2233}=0, b_{3333}=2, b_{1112}=0, b_{2212}=0, b_{3312}=0, b_{1212}=2, b_{1113}=0, b_{2213}=0, b_{3313}=0, b_{1213}=0, b_{1313}=2, b_{1123}=0, b_{2223}=0, b_{3323}=0, b_{1223}=0, b_{1323}=0, b_{2323}=1,c =2000

Passive inflation of an isotropic left ventricle model

b_{1111}=1**,** b_{1122}=0, b_{2222}=1, b_{1133}=0, b_{2233}=0, b_{3333}=1, b_{1112}=0, b_{2212}=0, b_{3312}=0, b_{1212}=0.5, b_{1113}=0, b_{2213}=0, b_{3313}=0, b_{1213}=0, b_{1313}=0.5, b_{1123}=0, b_{2223}=0, b_{3323}=0, b_{1223}=0, b_{1323}=0, b_{2323}=0.5,c =10000

Passive inflation of a fiber-reinforced left ventricle model

b_{1111}=8**,** b_{1122}=0, b_{2222}=2, b_{1133}=0, b_{2233}=0, b_{3333}=2, b_{1112}=0, b_{2212}=0, b_{3312}=0, b_{1212}=2, b_{1113}=0, b_{2213}=0, b_{3313}=0, b_{1213}=0, b_{1313}=2, b_{1123}=0, b_{2223}=0, b_{3323}=0, b_{1223}=0, b_{1323}=0, b_{2323}=1,c =2000